

CALIFORNIA STATE UNIVERSITY, NORTHRIDGE

INVESTIGATING THE RELATIONSHIP BETWEEN
STOKES' PROFILES AND LINE-OF-SIGHT
MAGNETIC FIELDS

A thesis submitted in partial fulfillment of the
requirements for the degree of Master of Science in
Physics

By

Max Norris

May 2014

The thesis of Max Norris is approved:

Ana Cristina Cadavid, Ph.D.

Date

Damian Christian, Ph.D.

Date

Debi-Prasad Choudhary, Ph.D., Committee Chair

Date

Acknowledgements

The author expresses his sincerest thanks to Dr. Debi-Prasad Choudhary's extensive help and insight. His encouragement and willingness to create opportunity has enabled both publication and travel, resulting in immeasurable experience. This thesis would not have been possible without any of his guidance. Also, to Dr. Ana Cadavid and Dr. Damian Christian for agreeing to be a part of the thesis committee. They were selected for personal reasons, and their acquiescence is noted and greatly appreciated. Furthermore, to all contacts within NSO and the SOLIS program, especially Dr. Alexei Pevtsov and John Britanik, whose donated time and knowledge contributed more than they are aware of.

Table of Contents

Signature Page	ii
Acknowledgments	iii
List of Figures	v
Abstract	vi
1 Introduction	1
1.1 Overview: The Solar Chromosphere	2
1.2 Magnetic Field Measurements	4
1.3 Stokes' Profiles Study	6
1.4 Review: CaII 8542 Å Study	8
1.5 Current Problem	9
2 Observational Data	10
2.1 VSM Instrument	11
2.2 Data Selection	12
3 Analysis	16
3.1 Technique	16
3.2 Equations and Interpretation	17
3.3 Error	21
4 Results	22
4.1 Asymmetry	22
4.2 Net Circular Polarization	33
4.3 Weak-Field Approximation	43
5 Conclusion	50
References	52
Appendix	55

List of Figures

Figure 1.1: Diagram of the solar structure.	3
Figure 1.2: Zeeman splitting.	5
Figure 1.3: Stokes parameters in degenerate states.	6
Figure 1.4: Example profiles of Stokes I and V.	7
Figure 1.5: Infrared calcium triplet.	8
Figure 2.1. NSO's SOLIS instrument.	10
Figure 2.2: Full-disk magnetogram; Sample of Stokes parameters.	11
Figure 2.3: Solar-Cycle 24.	14
Figure 2.4: LOS angle illustration.	15
Figure 3.1: Example of VSM Stokes I and resulting image.	16
Figure 3.2: Sample profiles used in calculations.	20
Figures 4.1 – 4.4: Stokes V with contour maps of asymmetry.	24
Figures 4.5 – 4.8: Asymmetry compared against LOS magnetic field.	29
Figures 4.9 – 4.12: Stokes V with contour maps of net circular polarization.	34
Figures 4.13 – 4.16: Net circular polarization versus LOS magnetic field.	40
Figure 4.17: Contour map of LOS magnetic field and gamma.	44
Figures 4.18 – 4.21: Gamma versus LOS magnetic field.	46

ABSTRACT

INVESTIGATING THE RELATIONSHIP BETWEEN STOKES' PROFILES AND LINE-OF-SIGHT MAGNETIC FIELDS

By

Max Norris

Master of Science in Physics

Using observations of Stokes I and V profiles of the CaII 8542 Å absorption line produced in the solar chromosphere, the magnetic and velocity properties of active regions are investigated. Results for several active regions in Solar-Cycle 24 with varying degrees of activity are presented. The studied properties include area and amplitude asymmetry, net circular polarization, and differences between Stokes V and the change in Stokes I with respect to wavelength ($dI/d\lambda$). These parameters are compared with the line-of-sight magnetic field, B_{LOS} , to determine their relationships. Data was acquired with the Vector Spectromagnetograph (VSM), operated by the National Solar Observatory's Synoptic Optical Long-term Investigations of the Sun telescope. The ground-based VSM provides Zeeman-induced Stokes profiles as well as the line-of-sight magnetograms from which B_{LOS} is inferred. Line asymmetries and net circular polarization are in agreement with expected spatial results, and similar dependences on B_{LOS} appear regardless of solar flare activity. Furthermore, it is concluded that Stokes V is proportional to B_{LOS} and $dI/d\lambda$.

Chapter 1

Introduction

The Sun's magnetic field is responsible for most, if not all, observed phenomena in solar physics. While these observations have been ongoing for centuries, their cause is a relatively recent discovery. It was just over one hundred years ago that George Ellery Hale observed magnetic signatures in sunspots. His 1908 experiment utilized a spectroscope to divide the Sun's incoming light into its component wavelengths emitted by different elements, or spectral lines. Previous spectroscopic experiments had revealed that some of these lines possessed doublets, or two spectral lines instead of just one. Hale, however, was the first to note that these doublets were of opposite polarity, indicating a magnetic origin [27]. Today, the division of one spectral line into multiple lines due to an external magnetic field is known as the Zeeman effect, or Zeeman Splitting.

Spectroscopy not only led to the discovery of the origin of sunspots, it is still being used to identify the sources of other, current solar anomalies. Together with similar Zeeman analysis as used by Hale, the most common way to infer information regarding magnetic fields from spectral lines is with the use of the Stokes parameters. These parameters describe the state of polarization of electromagnetic radiation as seen in the observed line profiles.

Stokes parameters can yield not only the strength of the magnetic field, but also its relative direction, inclination angle, velocity, and other useful data through various means and methods. More specifically and relative to this contribution is the line profiles' total amount of polarization, relative amount of "left" (blue) versus "right" (red) polarization, and the profiles' dependence on the magnetic field.

Higher understanding of the solar magnetic structure reveals how anomalies originate and why they occur in certain regions rather than others. Regardless of study, commonalities invariably arise involving systematic variations of Stokes polarization asymmetry across sunspots and their surrounding regions. By incorporating independent magnetograms, a more diversified method of associating the effect of magnetism on Stokes profiles is achieved. Finding direct connections between magnetic field strength and observed properties of Stokes profiles is of the utmost interest.

1.1. Overview: The Solar Chromosphere

The solar chromosphere is one of the most intriguing zones in the entire solar system. It is a 2000-kilometer thick region of plasma between the photosphere and the corona. In contrast to the photosphere, emission lines dominate the chromosphere. They are the key to studying this mysterious layer above the Sun and have provided insight into the Sun's atmospheric properties. The most prominent of these emissions is due to hydrogen-alpha, $H\alpha$, emitted at an unmistakably red 656.3 nm. Hence, the literal translation of the atmospheric layer's name: "sphere of color".

Due to the overwhelming brightness of the underlying regions, the chromosphere can only be observed directly during a total solar eclipse. Fortunately, alternative methods of observation have been devised, enabling scientific study. Of these methods, the most common is the practice of implementing a spectral filtering system, where filtering refers to eliminating light at all but certain wavelengths. If one can view specific portions of the spectrum, then different levels of the solar atmosphere may be viewed more independently of the others based on the light that is emitted there. Spectral filtering

during a total solar eclipse is even credited with providing the evidence necessary for the discovery of Helium in 1868 [17].

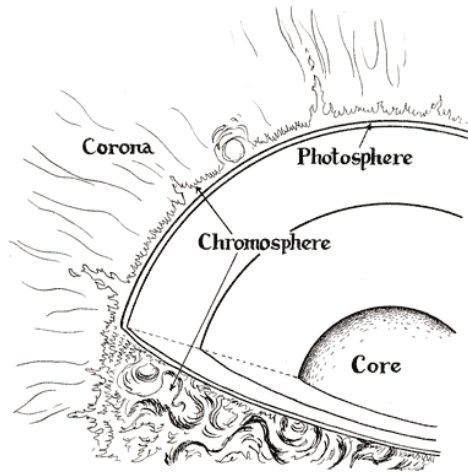


Figure 1.1: Diagram of the solar structure [18].

One of the many subjects of interest about the chromosphere is its temperature. The temperature in the chromosphere increases with distance away from the Sun and ranges from 6,000 to 50,000 degrees Kelvin. Current theories used to explain this phenomenon are mainly in terms of the magnetic field structure. The two most prominent classes are magnetic reconnection events to the surface (Parker 1988; Sturrock, 1999; Priest & Schrijver 1999) and heat caused by magnetic-field line vibrations, or magnetohydrodynamic (MHD) waves (Martinez-Sykora et al. 2011). More familiar magnetic components of the Sun, including spicules, flares, and prominences, also reside in the chromosphere and are believed to contribute to coronal heating as well. De Pontieu et al. (2011) and McIntosh et al. (2011) have recently shown how spicule dynamics make them ideal candidates in the quest for discovering efficient energy propagation into higher layers of the Sun's atmosphere (Jess et al. 2012).

Understanding the magnetic field within the solar atmosphere is not just a purely scientific goal; it is a practical one. Space weather caused by solar eruptions affects our satellites, astronauts, and electrical grids. Aside from scientific inquiry, the continuation of space exploration and electrical dependence has spiked the interest to learn as much as possible about the solar magnetic structure. Multiple efforts spanning the past five decades have commenced in order to further our understanding of the “solar dynamo” that fuels the Sun’s active regions and its weather. They are international, continuous, and very successful. With current technologies, solar physics is expanding at a record pace.

1.2. Magnetic Field Measurements

Global space agencies have produced space-based satellites dedicated to solar magnetic field observations. The National Oceanic and Atmospheric Administration (NOAA) operates the Geosynchronous Operational Environmental Satellite (GOES) to observe magnetic-field-related space weather. A joint mission between Japan, the United States, and the United Kingdom launched the spacecraft Hinode to explore the mechanisms that power the solar atmosphere and cause solar eruptions. In 2010, NASA launched the Solar Dynamics Observatory (SDO) equipped with its Helioseismic and Magnetic Imager (HMI) to produce continuous full-disk coverage at high spatial resolution [16].

Earthly atmospheric distortions to incoming electromagnetic radiation makes space-based observation of any celestial object preferable. However, ground-based telescopes have also played an important role in solar physics. The National Solar Observatory (NSO), in partnership with the Global Oscillation Network Group (GONG), oversees a worldwide network of observational telescopes with sites in several US states,

Australia, India, and Chile. These telescopes are capable of using the aforementioned spectral filters to observe specific spectral lines. From their observations of spectral anomalies, magnetic field strength and its properties can be discerned.

These anomalies include spectral lines that differ from expected profiles, which appear in the presence of an external magnetic field. The atoms, ions, or molecules producing the spectrum will be split into separate energy levels, in turn splitting their spectral lines. This split, or Zeeman effect, is proportional to the magnetic field strength. Thus, when anomalous spectra are observed, the magnetic field strength can be determined based on the amount of splitting [43]. This relationship is given by:

$$\Delta E = g_L \mu_B m_j B \quad (1.1)$$

where ΔE is the line's energy displacement from the zero-field level, g_L is the Lande g factor, μ_B is the Bohr magneton, m_j is the total angular momentum of the emitting atom/ion/molecule, and B is the external magnetic field strength [30].

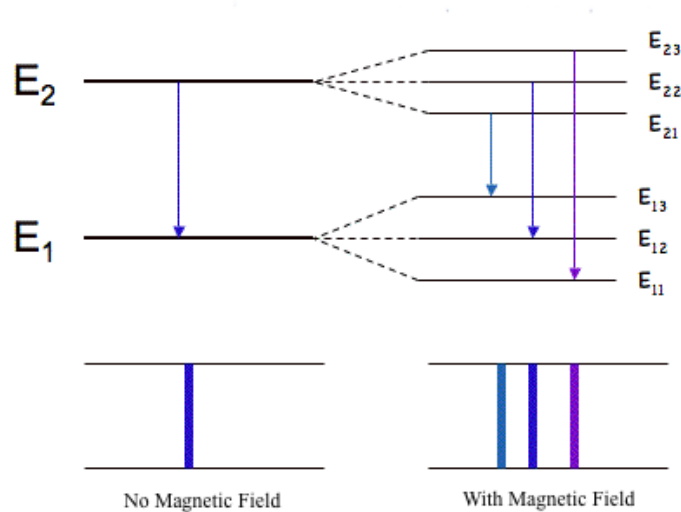


Figure 1.2: Zeeman splitting in the presence of an external magnetic field.

1.3. Stokes' Profiles Study

There are four polarization parameters of electromagnetic radiation: I, Q, U, and V. Familiar polarization states are circular and linear, which are degenerate cases of the general ellipse [41]. The two parameters that are used most often in research are the total intensity (I) and the circular polarization component (V).

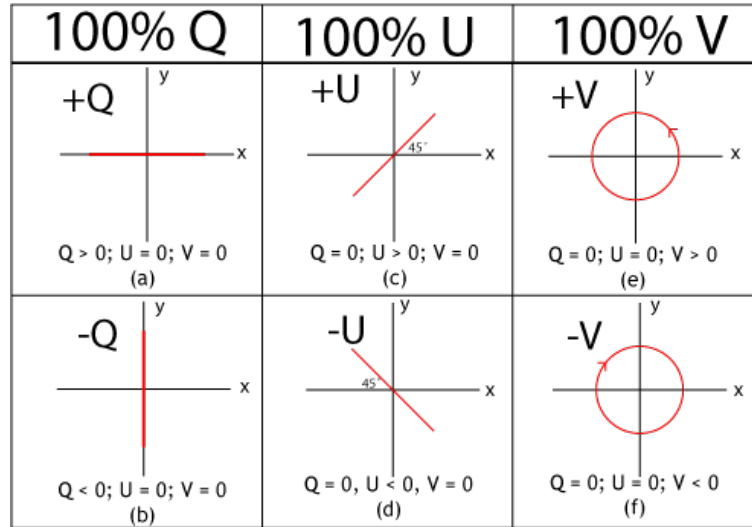


Figure 1.3: Stokes parameters in degenerate states [5].

Stokes profiles have been used to investigate the physical mechanisms that produce anomalous phenomena seen in absorption and emission spectra in the solar atmosphere. Balasubramanian, Keil, and Tomczyk (1997) determined that the center-of-gravity (COG) shifts of Stokes I indicate plasma velocities and found a systematic relationship between asymmetries in Stokes V and the presence of strong velocity fields. Navarro, Bueno, and Cobo (2000) focused on the time-dependence of asymmetries. They showed a periodic oscillation of ~ 150 s in the chromospheric lines between normal anti-symmetry and strong asymmetry. Choudhary, Balasubramanian, and Suematsu (2004) presented verification of the Evershed Effect based on velocity contours and Stokes V

asymmetries in and around sunspots. Their work showed “remarkable departures” between Stokes V within the umbra versus the surrounding region with opposite polarity.

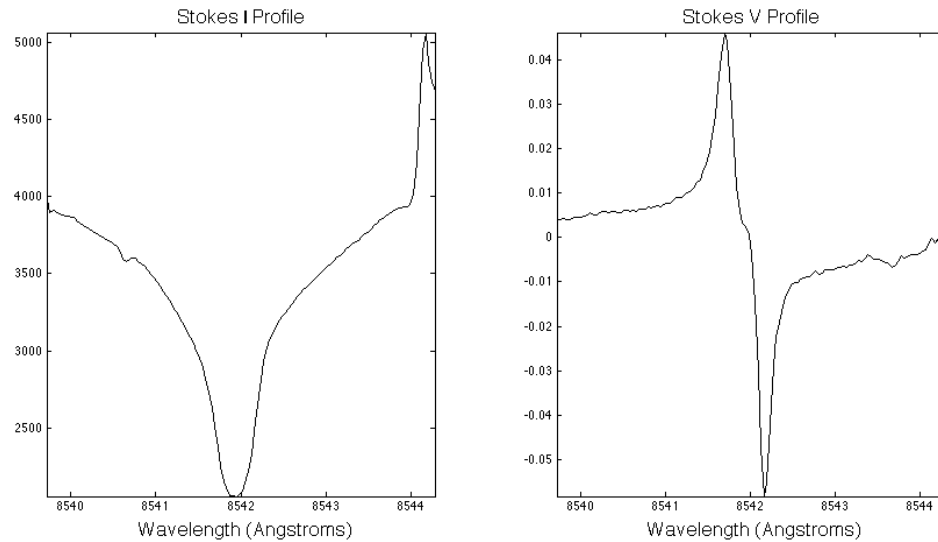


Figure 1.4: Example profiles of Stokes I and V from the same position within a sunspot.

Recent observations obtained with the High Altitude Observatory/National Solar Observatory’s (HAO/NSO) advanced Stokes polarimeter (Deng et al. 2010) analyzed simultaneous photospheric, FeI 6301.5 and 6302.5 Å, and chromospheric, MgI 5172.7 Å, lines. By using a two-component approach, a three-dimensional result showed that in plage regions where the “magnetic canopy” effect is present, Stokes V asymmetries are much higher in the photosphere than in the chromosphere.

A wide variety of information can be acquired via Stokes’ profiles. Asymmetry study and most other results are undoubtedly due to variations of the magnetic field in some form or another. Descriptions of these properties and their implications are discussed in Section 3.2.

1.4. Review: CaII 8542 Å Study

Spectral lines that originate in the chromosphere must be selected and filtered. These lines result from atomic energy-level transitions within the components of each atmospheric layer. One such chromospheric line is that of the ionized Calcium II isotope, emitting in the infrared at 8542 Å. This is an especially interesting profile to study. CaII 8542 Å is the most prominent profile of a triplet emission, ranging from 8498 to 8663 Å.

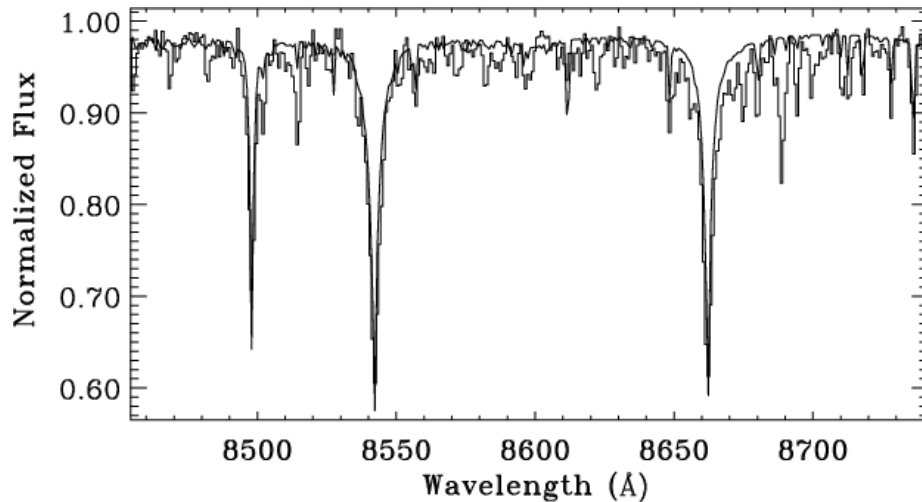


Figure 1.5: Infrared calcium triplet (Aznar Cuadro & Jeffrey, 2002).

Existing research has used the calcium triplet to observe atomic collisional broadening and the usefulness of triplets in general to indicate stellar luminosity (Smith & Drake, 1988). A unique trait of value in the calcium triplet is the difference in origin of the profile's "core" and "wings". The core of the profile, within ± 1 Å of line center, is formed in the chromosphere, whereas the wings are formed in the lower photosphere (Smith & Drake, 1988 and references therein). This allows for simultaneous comparison and improves our understanding of the interaction between the two regions.

Triplets are also ideal for measuring variations in physical quantities with varying height in the solar atmosphere. Each line profile within the calcium triplet is formed at

different heights, and each is strong enough to yield reliable data. This permits three-dimensional modeling of velocity gradients, magnetic canopies, and Evershed flows without having to use separate atomic spectra.

1.5. Current Problem

Underlying the plethora of results and conclusions offered by the many submissions of research in solar physics and chromospheric magnetic fields, direct quantitative links between the line-of-sight (LOS) magnetic field and its role in producing observed Stokes profiles is missing. Jack Harvey produced such a relationship in his work with NSO and NOAA (Harvey, 1985). Two goals must then be met: (1) Confirming previous asymmetry and net circular polarization results to ensure data acquisition and its use is reliable; and (2) finding straightforward connections with the LOS magnetic field (B_{LOS}) and observed profiles using Harvey's weak-field approximation method.

Chapter 2

Observational Data

Chromospheric full-disk LOS magnetograms and Zeeman-induced Stokes profiles for active regions NOAA 11356, 11401, 11640, and 11667 were provided by NSO's Synoptic Optical Long-term Investigations of the Sun (SOLIS). The goal of SOLIS is to better understand the solar activity cycle, solar eruptions, and the role of solar radiation changes with respect to global climate change [26]. SOLIS is composed of a single equatorial mount (Balasubramanian & Pevstov, 2011), as seen in Figure 2.1. It carries three telescopes: the 50 cm Vector Spectromagnetograph (VSM), the 14 cm Full-Disk Patrol (FDP), and the 8 mm Integrated Sunlight Spectrometer (ISS).



Figure 2.1. NSO's SOLIS telescope located atop the Kitt Peak Vacuum Telescope.

Vector magnetograms are synoptic maps representing LOS magnetic fields and have been previously derived by SOLIS. They are single images per day. Stokes profiles are not. These large data sets must be read and converted in order to be used. Thus, separate data sets from the same instrument allows for direct calculations and comparison between magnetograms and the Stokes profiles.

2.1. VSM Instrument

The VSM is designed to obtain “high-quality magnetic field observations in the photosphere and chromosphere by recording the Zeeman-induced polarization of spectral lines...” [26]. It records the Zeeman-induced polarized Fraunhofer lines in photospheric and chromospheric CaII 8542 Å with a spatial resolution of 1 arc second per pixel. Stokes profiles of active regions using the magnetically sensitive CaII 8542 Å line are in the range of 8542 ± 2.275 Å. The solar image is recorded using a Littrow spectrograph, with the slit covering 2048 arc seconds. Three individual LCD polarization modulators derive the LOS polarimetry for the CaII 8542 Å wavelength ranges. Both solar hemispheres are recorded simultaneously by splitting the 2048 arc second image with a focal-beam splitter, where each is reimaged into two separate CCD cameras of 1024 x 512 pixels. Both cameras take data in two orthogonal polarization states. Complete solar images are taken by moving the telescope in declination, which are then scanned to create full-disk magnetograms [26]. The figures below show examples of the magnetograms and VSM spectra.

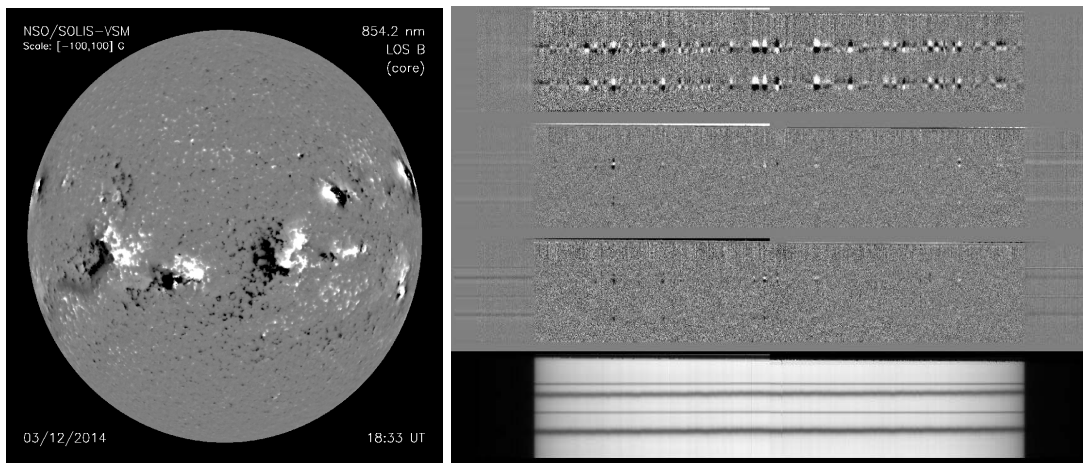


Figure 2.2: Full-disk magnetogram taken by the VSM (left). Sample of Stokes parameters provided by the VSM (right). V, Q, U, and I are shown from top to bottom [26].

2.2. Data Selection

This contribution means to compare and verify existing properties of Stokes profiles, along with creating new means of correlating them with LOS magnetic fields. For this purpose, a range of regions, dates, and activity is desired. Diversity of data will strengthen results and give a broader view of any resulting relationships. Throughout Solar-Cycle 24, dates and regions were therefore selected based on location within the cycle, regional activity, and availability. Activity and region location on the solar disk are supplied courtesy of SolarMonitor.org and are listed in Table 1.

Table 1
Sunspot and Region Information

NOAA Region	Date	Location	Radial Distance (R_{\odot})	Activity (flares)
<i>11356</i>	11/22/11	N15, E41	0.485	9 C-Class
	11/23/11	N15, E28	0.353	1 C-Class
	11/27/11	N16, W24	0.320	No Flares
<i>11401</i>	1/18/12	N18, E24	0.333	2 C, 1 M-Class
	1/19/12	N16, E13	0.229	1 C-Class
	1/23/12	N16, W40	0.479	1 C-Class
<i>11640</i>	1/2/13	N28, W20	0.382	No Flares
	1/3/13	N28, W35	0.498	1 C-Class
<i>11667</i>	2/5/13	N22, E14	0.290	No Flares
	2/6/13	N22, W00	0.244	1 C-Class

The radial distance is given in units of solar radii (R_{\odot}), and is an approximation given by:

$$r = \sqrt{\left(\frac{NS^{\circ}}{90^{\circ}}\right)^2 + \left(\frac{EW^{\circ}}{90^{\circ}}\right)^2} \quad (2.1)$$

where the NS° and EW° are the north-south coordinates and east-west coordinates, respectively. The value for radial distance is stated as an approximation because it is assumed that observed longitude and latitude coordinates extend linearly from the disk center, which is not the case. This error is not taken into account because r is used simply for qualitative analysis and does not appear in future calculations.

Apparent from Table 1 is the variety of data. The set spans approximately 14 months, $r \sim 0.2 - 0.5 R_{\odot}$, and contains quiet regions with little flare activity to the hyperactive. Varying dates may be seen as a factor of observational data and results. As the solar-cycle progresses, the number of sunspots increases towards maximum, indicating an increase in magnetic flux. Selecting sunspots throughout the cycle may provide differences in both Stokes profile properties as well as their interaction with magnetic field strength. The dates used are scattered throughout the rising phase of the current cycle:

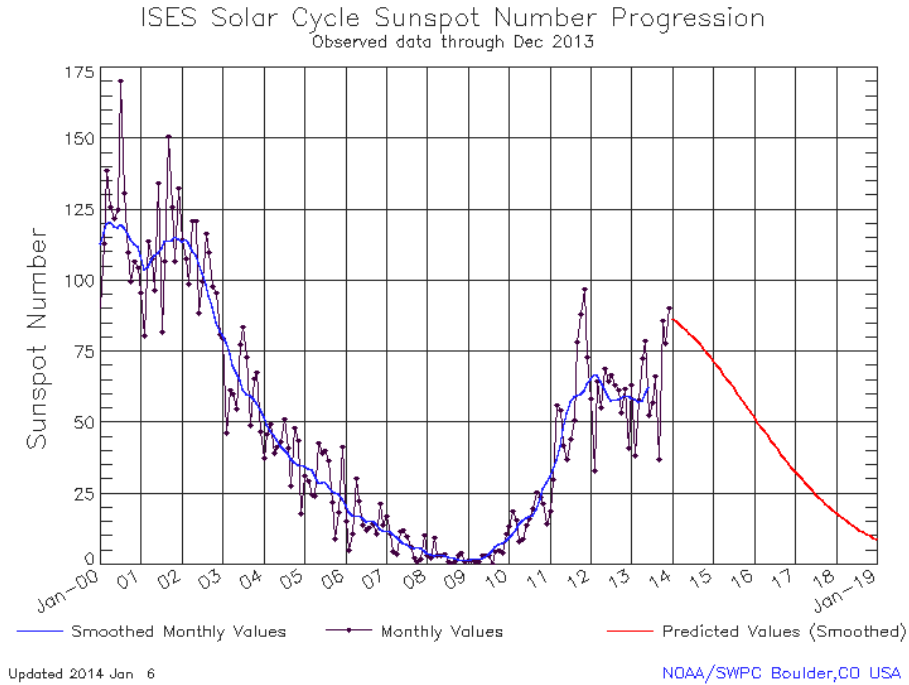


Figure 2.3: Solar-Cycle 24

Radial distance plays a major role in the LOS angle. Sunspots near or at disk center will have a more direct LOS angle to the observer than sunspots observed at the edge. This affects the observed magnetic field as well as observed Stokes profiles. What needs to be measured is the magnitude this effect has on asymmetry and/or net circular polarization. Within these two quantities, there are several well-known distinctions between the polarities of surrounding sunspot regions that face disk-center and those that face disk-limb. Location on the solar disk is therefore a factor in analyzing parameter outcomes.

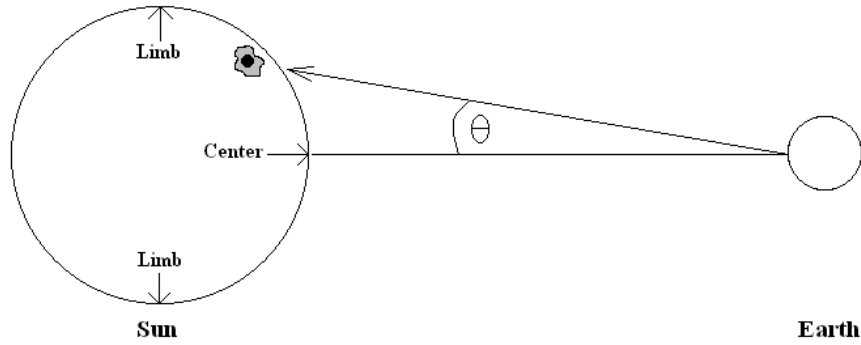


Figure 2.4: LOS angle illustration.

The focus, however, is to compare results in regions with high activity to the results from low activity regions. By defining activity as the number of solar flares, it is also defined as the amount of relative magnetic activity. NASA defines a solar flare as “an intense burst of radiation coming from the release of magnetic energy...” [34]. Thus, the expectation is to see a more dramatic effect on derived quantities that are affected by the magnetic field during days with high activity versus those with low activity.

Chapter 3

Analysis

NSO data is highly accurate and reliable. It is used in countless publications and is one of the great data acquisition systems with respect to solar physics. Its accessibility and tremendous catalog size were the final influences for utilizing its resources as opposed to personally collecting original data.

3.1. Technique

Data files and folders were read directly into MatLab via coding developed for this project. All coding necessary for input and calculations is provided in the Appendix. As stated in the previous chapter, pixels relating to spatial points on the solar disk each have an associated V and I profile, spanning $8542 \pm 2.275 \text{ \AA}$. An example of the provided data is shown in Figure 3.1.

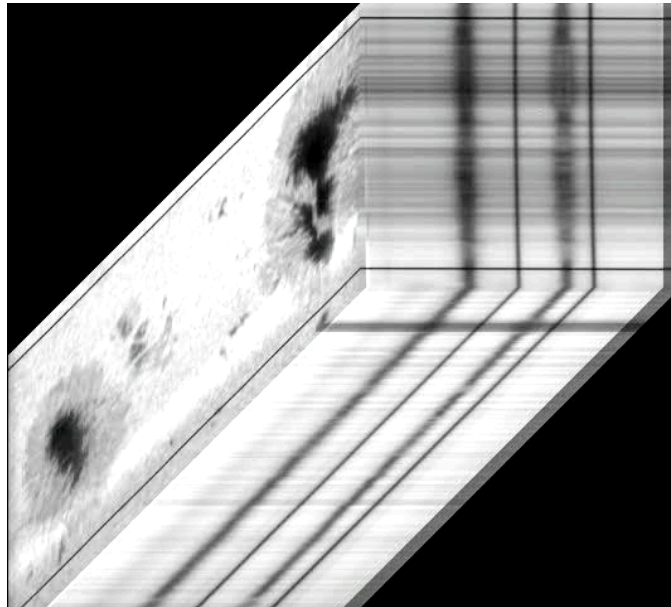


Figure 3.1: Example of VSM Stokes I and resulting image [15].

3.2 Equations and Interpretation

All quantities except for B_{LOS} were calculated using the observed Stokes I and V. In contrast to previous methods, normalization to the quiet-Sun continuum was neglected for better comparison with local magnetic fields. Each VSM image consisted of 2047 files, scanning the solar disk through 128 wavelengths. After manipulation, a daily image based on the average value of all 128 wavelengths is produced. Spatial points of interest may be selected to yield both I and V profiles. To achieve more accurate results, all profiles are interpolated by a factor of 100. This method is used only to pinpoint specific wavelengths, such as zero-crossings, and in no way affects asymmetry or other calculations.

These quantities' calculations and interpretations are based upon both existing and original methods. They are explained as follows:

1. *Stokes V Amplitude and Area Asymmetries.*

Asymmetry of solar line profiles has been studied for several decades and has given researchers a wealth of information. It has been shown to reveal gradients in both velocity and magnetic fields. In the same fashion as Doppler analysis, shifting asymmetry to either positive or negative wavelengths with respect to the theoretical center indicates the gradients' motion (Solanki, 1986). Since Stokes V only has contributions from magnetized plasma (Deng et al. 2010), it is a useful and appropriate tool in the investigation of chromospheric magnetic fields.

Peak values of the blue and red lobes, b and r , are determined. The areas of the blue and red lobes are calculated by integrating V over the left and right wings of the zero-crossing wavelength, λ_z , respectively. Following Solanki & Stenflo (1984),

Balasubramaniam et al. (1997), and Deng et al. (2010), the percentages of amplitude asymmetry, a , and area asymmetry, A , are derived:

$$\delta a = 100 \times \frac{|b| - |r|}{|b| + |r|} \quad (3.1)$$

$$\delta A = 100 \times \frac{(B - R)}{(B + R)} \quad (3.2)$$

where

$$B = \int_{\lambda_i}^{\lambda_z} |V(\lambda)| d\lambda \quad (3.3)$$

$$R = \int_{\lambda_z}^{\lambda_f} |V(\lambda)| d\lambda \quad (3.4)$$

Area asymmetry will prove to be indicative of the total amount of positive or negative polarization. To compare, a value for net circular polarization, n_{cp} , (Gosain & Choudhary, 2003) and normalized net circular polarization, NCP , are introduced.

2. *Net Circular Polarization*

Net circular polarization is a means to measure the total amount of asymmetry and polarization in Stokes V profiles due to the magnetic field and the Zeeman effect. It also suggests magnetic polarity. Since net circular polarization depends on the presence of asymmetry, it too requires velocity and magnetic field gradients. One then expects similar patterns to appear between the two values. In fact, there are many established qualities shared by each including their spatial distributions and polarity near sunspots and neutral lines. The effects of asymmetry and net circular polarization will be shown and compared to previous findings in Chapter 5. In agreement with Gosain & Choudhary (2003), n_{cp} is defined as:

$$n_{cp} = \int_{\lambda_i}^{\lambda_f} V(\lambda) d\lambda \quad (3.5)$$

Furthermore, to examine polarization more independently of B_{LOS} , a normalized net circular polarization, NCP, is introduced in which Stokes V is locally normalized:

$$NCP = \frac{\int_{\lambda_i}^{\lambda_f} V(\lambda) d\lambda}{\max(|V(\lambda)|)} \quad (3.6)$$

3. *Weak-Field Approximation*

Based on J. Harvey's "Trends in Measurement of Solar Vector Magnetic Fields Using the Zeeman Effect", a relationship is found between Stokes V, B_{LOS} , and Stokes I. They are related by a constant, k, such that

$$V(\lambda) = k * B * \cos(\theta) * \frac{dI(\lambda)}{d\lambda} \quad (3.7)$$

where B is the magnetic field strength and θ is the LOS angle. By defining a quantity gamma, Γ , k can be easily computed:

$$\Gamma(\lambda) \equiv \frac{V(\lambda)}{I'(\lambda)} \quad (3.8)$$

$$k = \frac{\Gamma}{B_{LOS}} \quad (3.9)$$

Two average values of Γ will be computed for each spatial point: region, Γ_R , and peak, Γ_P . Both values of Γ are determined from a specific wavelength range that is dependent upon λ_z for the umbra ($\lambda_{z,U}$), penumbra ($\lambda_{z,P}$), and quiet Sun ($\lambda_{z,Q}$) for each respective day:

$$\lambda_1 = \langle \lambda_{z,U} | \lambda_{z,P} | \lambda_{z,Q} \rangle - 0.3583 \text{ \AA} \quad (3.10)$$

$$\lambda_2 = \{ \lambda_{z,U} | \lambda_{z,P} | \lambda_{z,Q} \} + 0.3583 \text{ \AA} \quad (3.11)$$

where the operators $\langle X \rangle$ and $\{Y\}$ return the minimum and maximum values, respectively.

Γ_R and Γ_P may now be calculated:

$$\Gamma_R = \frac{\int_{\lambda_1}^{\lambda_2} \Gamma(\lambda) d\lambda}{(\lambda_2 - \lambda_1)} \quad (3.12)$$

$$\Gamma_P = \frac{|\Gamma_{p1}| + |\Gamma_{p2}|}{2} \quad (3.9)$$

where Γ_{p1} and Γ_{p2} and the peak Γ values in the set wavelength range.

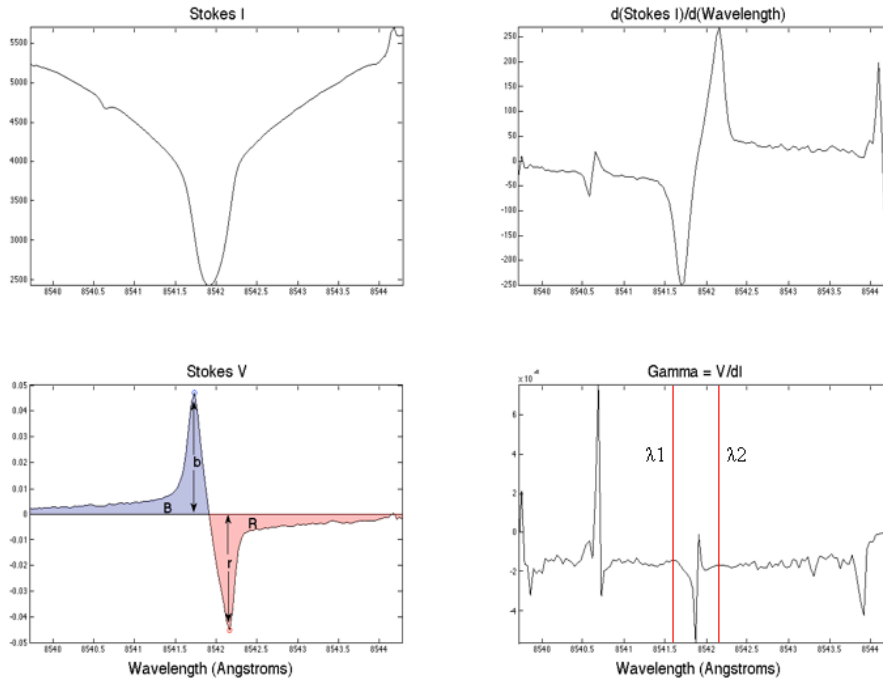


Figure 3.2: Sample profiles used in calculations.

3.3 Error

By employing a globally recognized source, error in measurement has been minimized by eliminating those involved in taking personal data. There are known issues for the VSM which are listed by NSO: (1) Certain locations near neutral lines or plages have field strength readings that are too high; (2) field strengths within the umbra are sometimes lower than expected; and (3) quiet Sun field inclination angles are biased towards the transverse direction [26]. These cannot be avoided and only affect a very small percentage of the total data. The above calculations therefore have the same precision as those in other works that use VSM data.

In the calculated quantities, there are few differences in technique from their cited origins. Balasubramanian et al. (1997) noted that the definition of peak amplitude asymmetry, equation 3.1, breaks down when Stokes V contains multiple reversals, which can occur near magnetic neutral lines. A threshold of 300 Gauss (G) was enacted to avoid such profiles. This contribution did not observe such thresholds. Gosain & Choudhary (2003) and Deng et al. (2010) also avoided B_{LOS} thresholds. Comparison with multiple sources may reveal if error is present.

Further deviation from previous methods resides with Stokes I. Many authors have chosen to normalize observed profiles to the local continuum, $I(\lambda) = I(\lambda)_{\text{observed}} / I_c$ and $V(\lambda) = V(\lambda)_{\text{observed}} / I_c$ (Socas-Navarro et al. 2000; Gosain & Choudhary, 2003; Deng et al. 2010). Effects of this normalization will only appear in ncp. Qualitative analysis for ncp is luckily unaffected. Spatial comparison is still achievable without accounting for the local continuum, as its effect would be constant throughout the region.

Chapter 4

Results and Discussion

4.1 Asymmetry

Amplitude and area asymmetries are shown in Figures 4.1 through 4.4. Limb-side penumbrae display opposite asymmetry polarity as center-side penumbrae. This is in agreement with existing results (Choudhary et al. 2004; Deng et al. 2010; Beck, 2013) and can be seen in both contour map and scatter plot findings for δa and δA . Observations by Balasubramanian et al. in 1997 concluded that no relationship exists between Stokes V amplitude asymmetries and B_{LOS} . From the presented images, both correlated and uncorrelated cases are seen. Figures 4.1 and 4.2 display clear distinctions between (1) sunspot and surrounding region and (2) daily activity. The converse is true for Figures 4.3 and 4.4. A reversal of correlation is seen, with less solar flare activity yielding higher asymmetries. Higher solar flare activity results in more asymmetry and better agreement with existing findings. During low activity, other factors within the solar atmosphere must be primarily responsible for the gradients that produce observed asymmetries. These factors include transition region heating (Martinez-Sykora et al. 2011), mixed polarities (Deng et al. 2010 & Sigwarth 2001), inclined flux tubes (Choudhary et al. 2004 & Grossman-Doerth et al. 2000), and other related phenomena.

An obvious redshift in amplitude asymmetry in the umbra is also noted. In all four asymmetry Figures, contour maps with the most distinct asymmetries show positive (blue) values in the limb-side penumbra and plage regions, and negative (red) values near the center of the sunspot and center-side penumbra, regardless of sunspot polarity. This characteristic has been noted by nearly all cited references and is largely due to the

observer's line-of sight view of the Evershed flow (Almeida & Lites, 1992). Since the values used for amplitude asymmetry, b and r , are associated with the V profile's chromospheric contribution, these contour maps give direct insight to the flow dynamics of the chromosphere. Umbrae and center-side penumbrae display matching amplitude asymmetry because the inward flow from penumbrae towards the umbrae appear to be moving away from the observer in these regions. The limb-sides' inward flow appears to be coming towards the observer, thus yielding blue asymmetry.

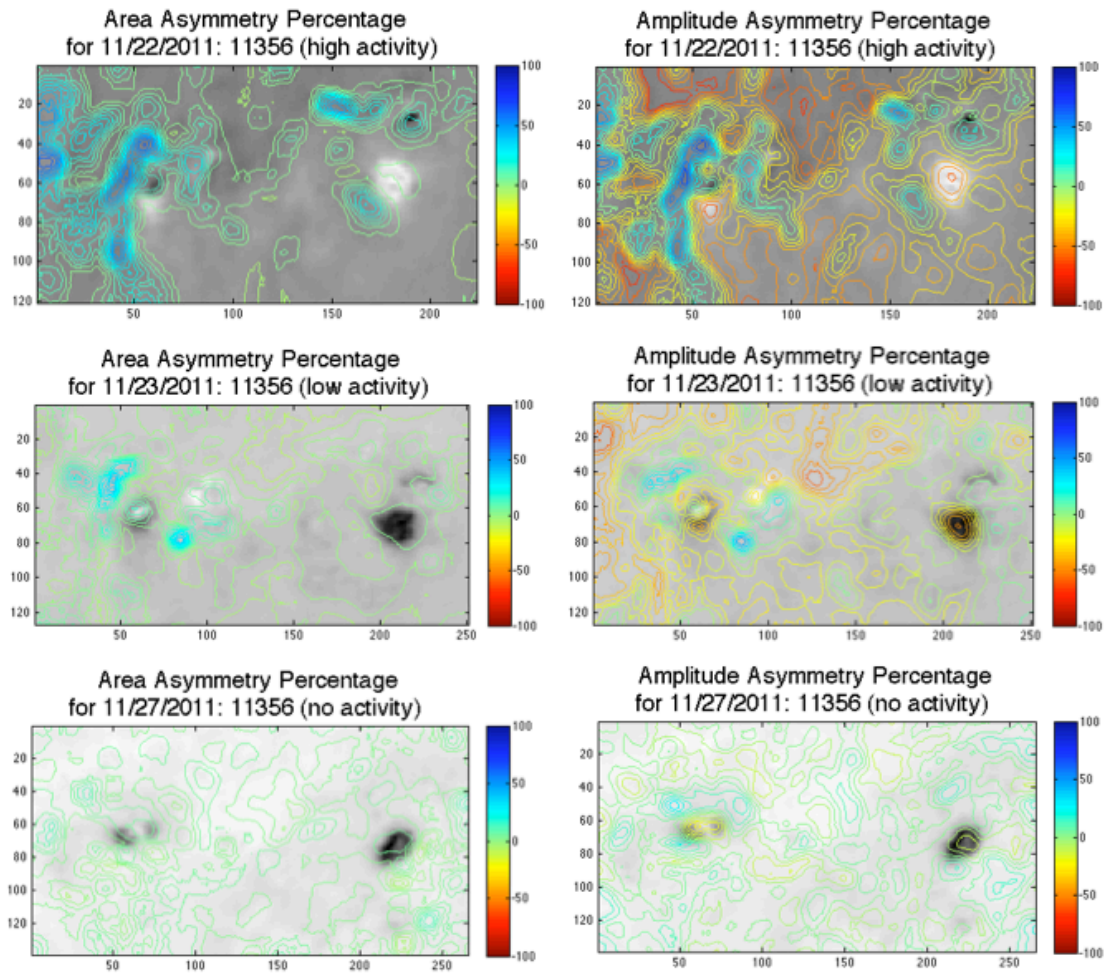


Figure 4.1: Images constructed of NOAA 11356 from Stokes V with contour maps of asymmetry corresponding to spatial points for three separate days and activity. Disk-center is to the right, right, and top left for the three sets of images, respectively. The white and black regions of the V image represent positive and negative polarities, respectively. The contour maps are consistent in range from -100% (completely red) to 100% (completely blue).

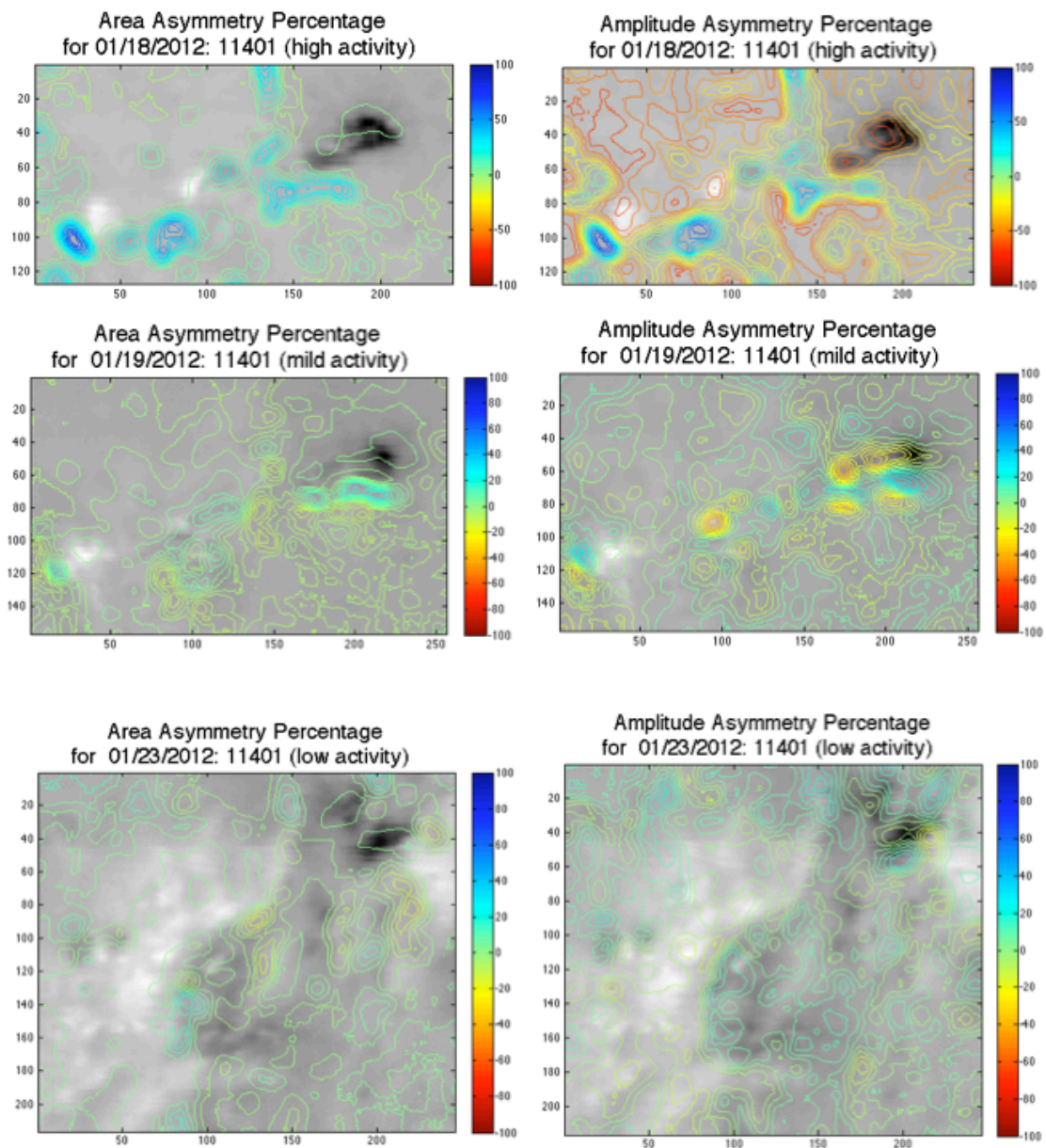


Figure 4.2: Images constructed of NOAA 11401 from Stokes V with contour maps of asymmetry corresponding to spatial points for three separate days and activity. Disk-center is to the top right, top right, and top left for the three sets of images, respectively.

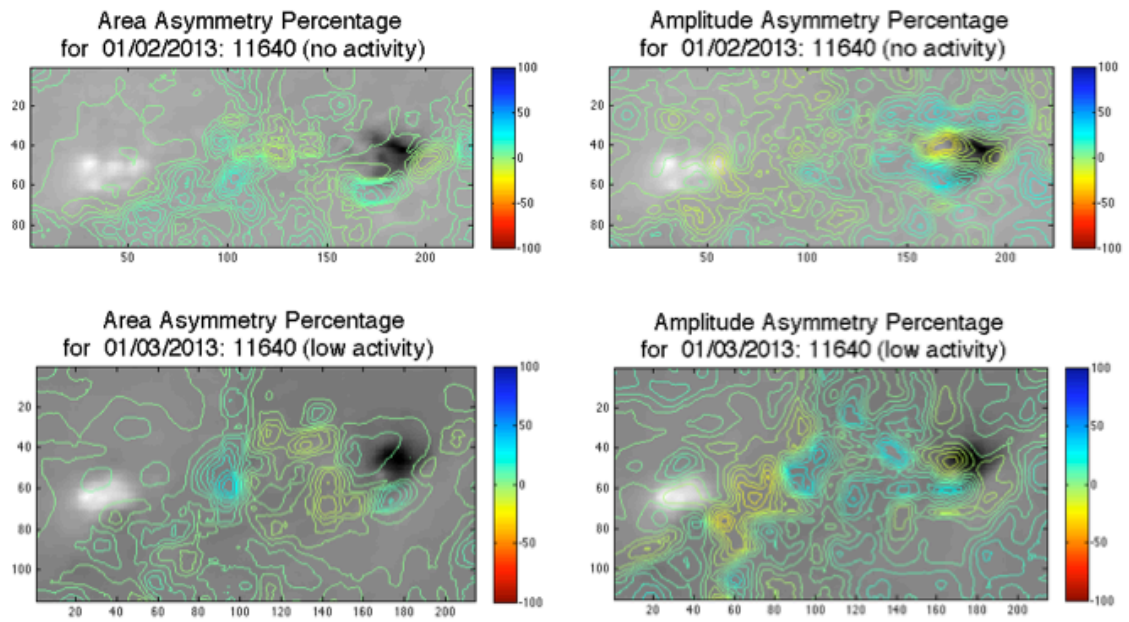


Figure 4.3: Images constructed of NOAA 11640 from Stokes V with contour maps of asymmetry corresponding to spatial points for two separate days and activity. Disk-center is to the top left for both sets of images.

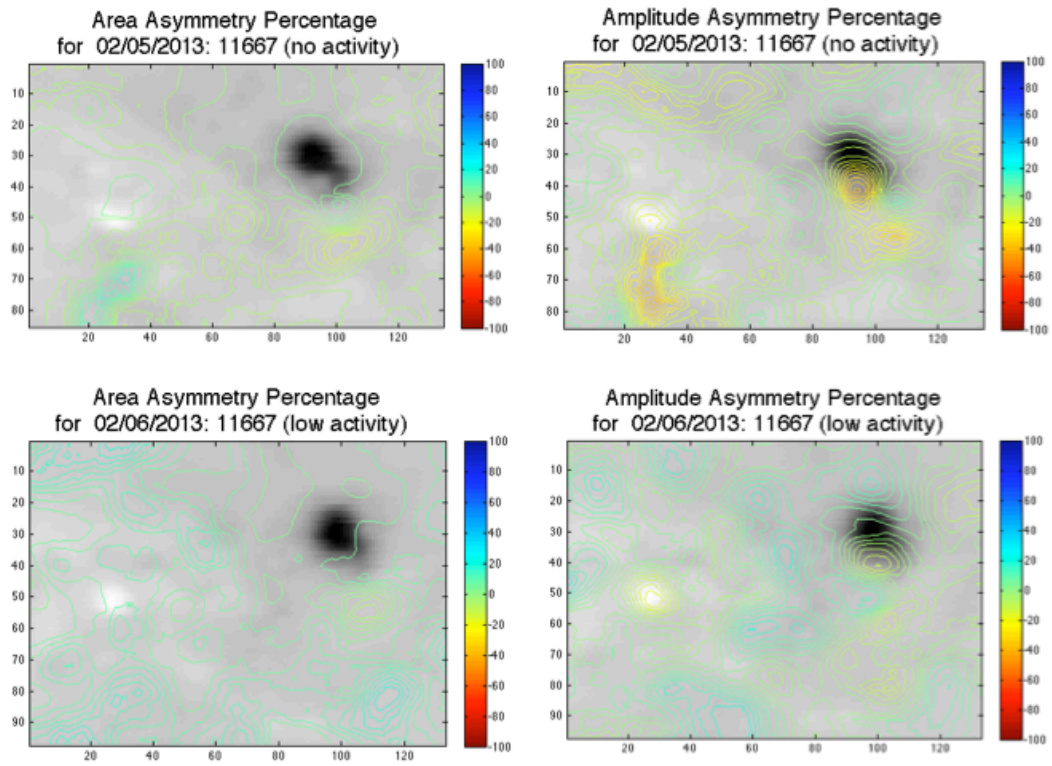


Figure 4.4: Images constructed of NOAA 11667 from Stokes V with contour maps of asymmetry corresponding to spatial points for two separate days and activity. Disk-center is to the top right, and directly upwards for the two sets of images, respectively.

To analyze any relationship between Stokes V asymmetries and B_{LOS} quantitatively, pixel-to-pixel spatial values are compared in scatter plots as seen in Figures 4.5 through 4.8. As expected, higher magnetic fields produce less area asymmetry, or more anti-symmetry, of the blue and red lobes than lower magnetic fields within quiet regions. Large Zeeman splitting of the CaII 8542 Å line in strong fields is a likely cause for small area asymmetries (Deng et al. 2010 & Grossman-Doerth et al. 1989). Near the 0 G neutral lines, the higher activity scatter plots reveal a “fountain” effect towards the positive direction, appearing blue in the contour maps. There has been preceding evidence showing that near the neutral lines, Stokes V is at a minimum and leads to large asymmetry values (Almeida & Lites, 1992).

Amplitude asymmetry appears unassociated with B_{LOS} upon first glance, but actually strengthens existing observations and hypotheses. The Figures below demonstrate strong negative (red) amplitude asymmetries for large field strengths ($|B_{LOS}| \geq 400$ G). This is indicative of umbrae with “higher” yet narrower red lobes and is concluded by multiple works regarding asymmetry across active regions (Almeida & Lites, 1992; Balasubramanian et al. 1997; Gosain & Choudhary, 2003). Days with higher solar flare activity also display the same fountain effect present as seen in area asymmetry. The departure from negative to positive polarization about the $B_{LOS} = 0$ G neutral line for both area and amplitude asymmetry may not be entirely dependent on the LOS angle. A more probable origin is a dual contribution from the magnetic and velocity field reversals near the neutral line along increasing LOS angles.

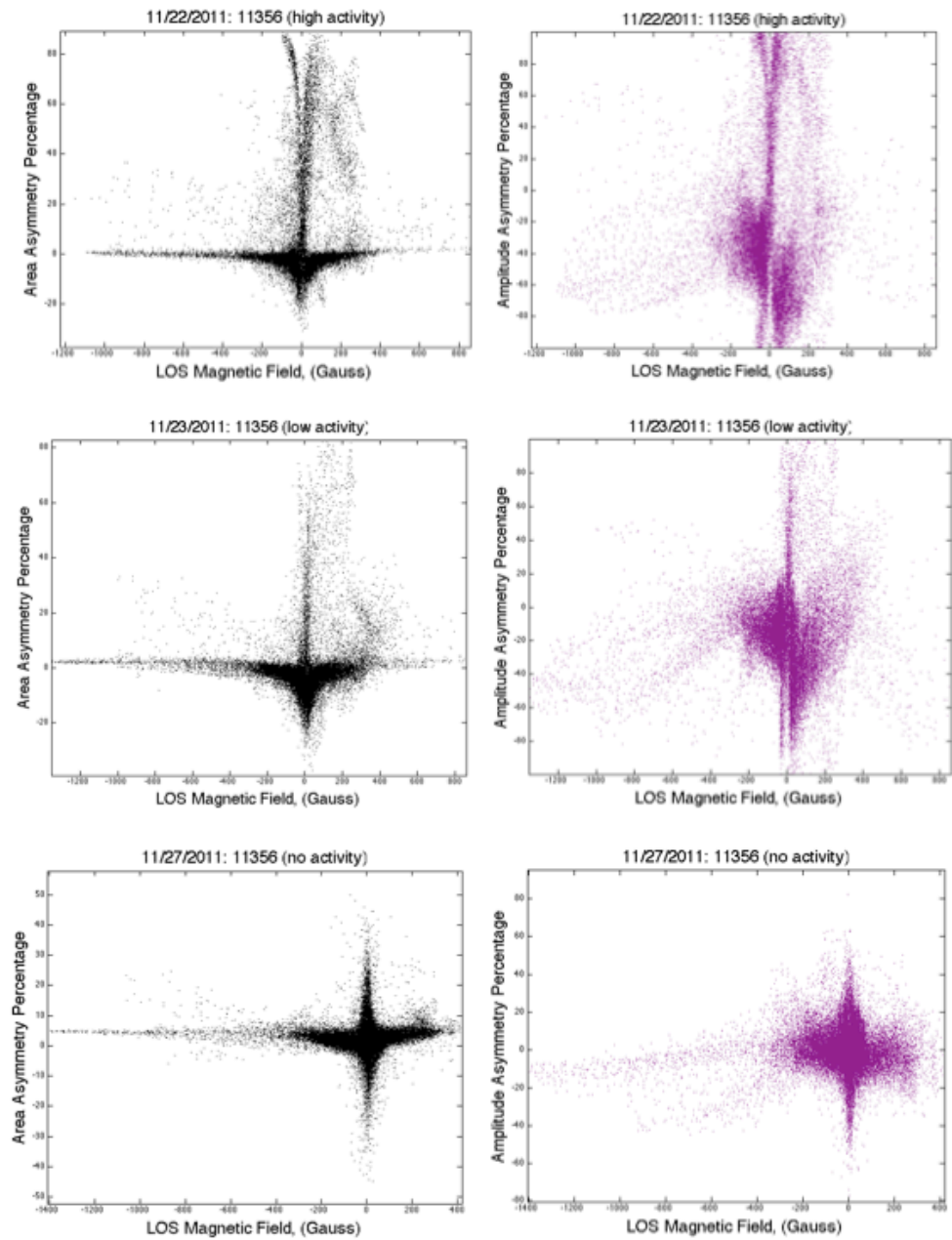


Figure 4.5: Derived asymmetries of NOAA 11356 from Stokes V directly compared against VSM magnetogram line-of-sight magnetic field.

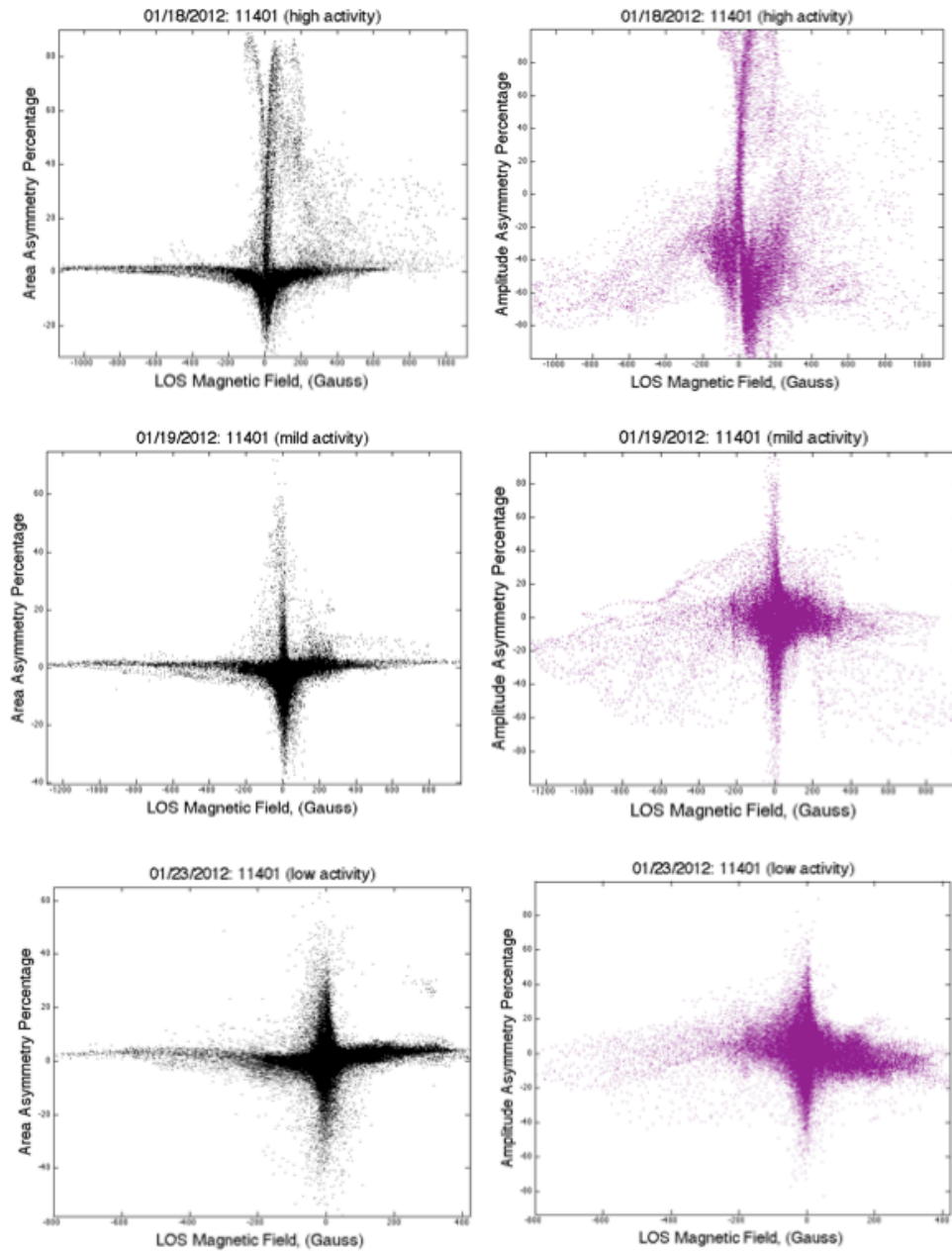


Figure 4.6: Derived asymmetries of NOAA 11401 from Stokes V directly compared against VSM magnetogram line-of-sight magnetic field.

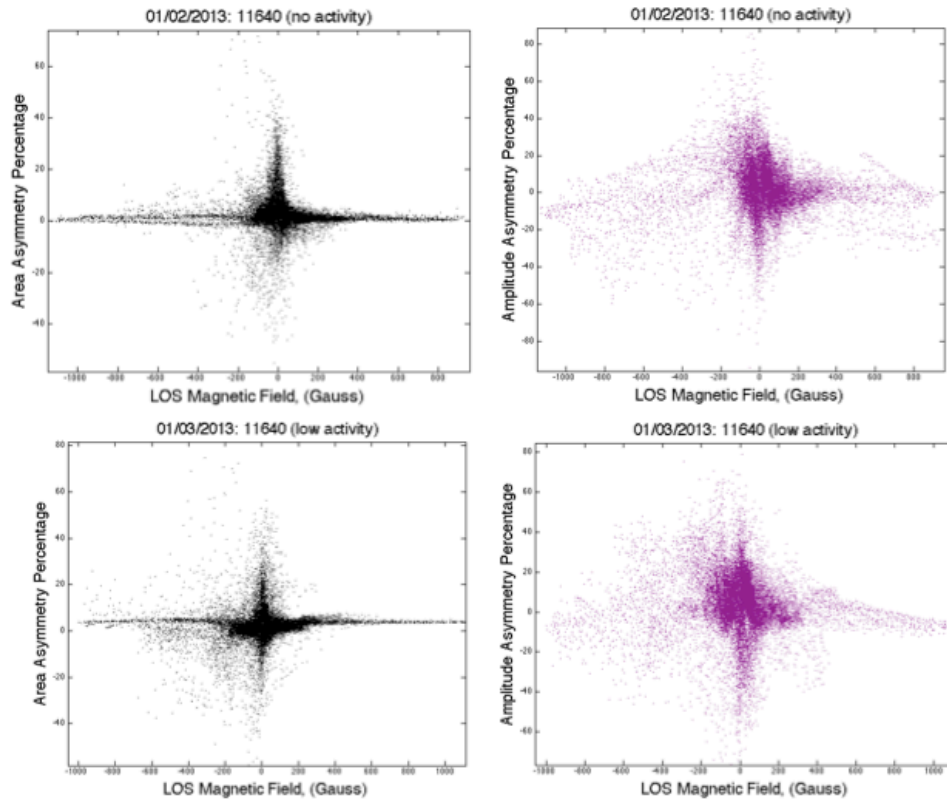


Figure 4.7: Derived asymmetries of NOAA 11640 from Stokes V directly compared against VSM magnetogram line-of-sight magnetic field.

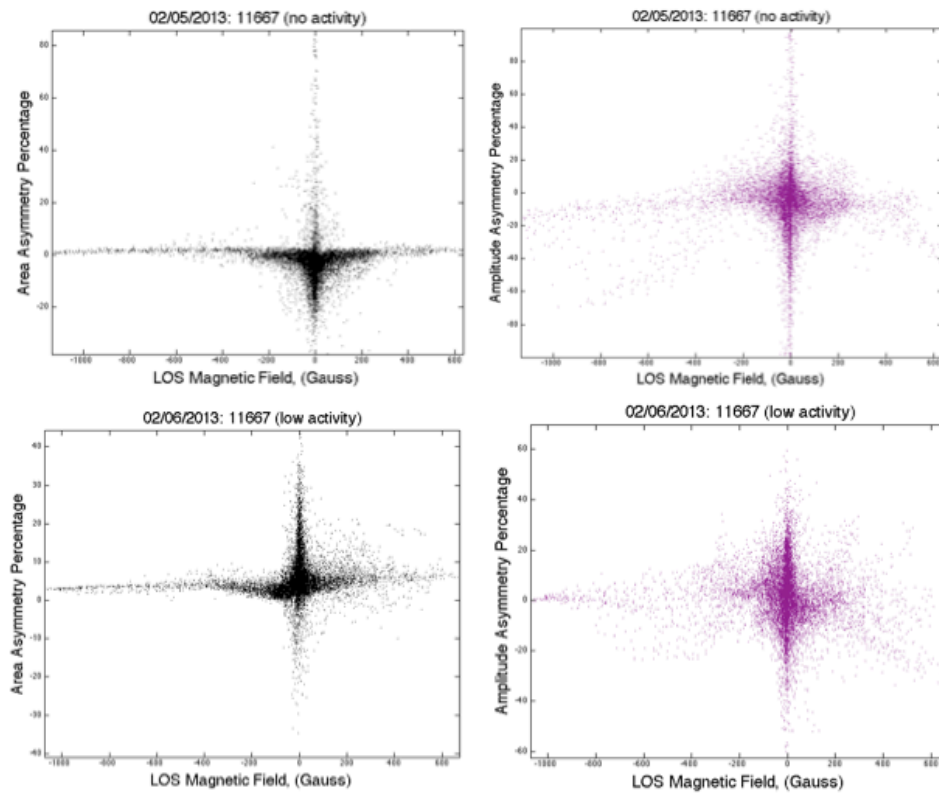


Figure 4.8: Derived asymmetries of NOAA 11667 from Stokes V directly compared against VSM magnetogram line-of-sight magnetic field.

4.2 Net Circular Polarization

Net circular polarization is a simple way to characterize Stokes V asymmetry (Tritschler et al. 2007) and represents its spatial distribution (Gosain & Choudhary, 2003). Similar to asymmetries, LOS gradients in velocity and magnetic field are required to generate observed ncp (Almeida & Lites, 1992). Also, the more interesting aspects of ncp occur in the penumbrae due to a variety of magnetic and velocity field variations along the LOS. Some of the more recognized suggestions for the three-dimensional organization of penumbral magnetic fields that lead to said aspects are described by Beck (2013) and references therein: (1) “uncombed” penumbra where less inclined field lines wind around horizontal flow channels; (2) micro-structured magnetic atmosphere, MISMA, with fine structures of the magnetic field at a few kilometers; (3) magnetic flux pumping; and (4) field-free gaps with convective motions below the visible surface. Beck (2013) and Borrero et al. (2007) have both employed uncombed inversion techniques to explain the three-dimensional topology and to reproduce observed ncp with great accuracy.

Visual evidence is presented to support the above findings along with several others. Maps of ncp and NCP are shown in Figures 4.9 through 4.12. They show strong agreement with previous conclusions and the above asymmetry results. Center and limb-side penumbra are of opposite sign in both ncp and NCP, with center-side showing more positive values and limb-side showing more negative. This, however, is in contrast to Gosain & Choudhary (2003) who found center and limb-sides to have negative and positive values, respectively. In high solar flare activity maps, the symmetric nature of ncp about the line connecting disk-center to sunspot-center is visible, as found by

Tritschler et al. (2007) and Almeida & Lites (1992) in the FeI 6302.5 Å line. Upon close examination, it is clear in the NCP maps that the center-side penumbra not only has opposing sign than the limb-side, but smaller absolute value. This is in complete agreement with findings by Almeida & Lites (1992).

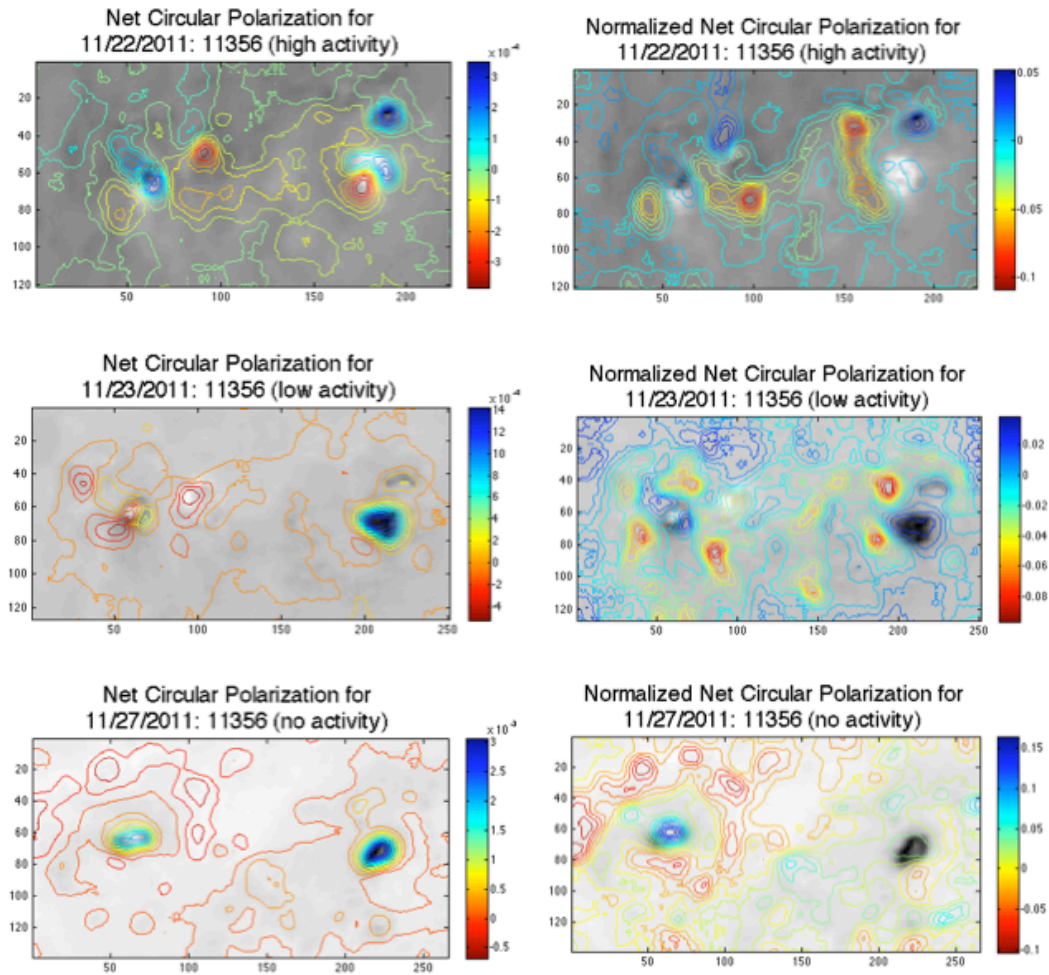


Figure 4.9: Images constructed of NOAA 11356 from Stokes V with contour maps of net circular polarization corresponding to spatial points for three separate days and activity. Disk-center is to the right, right, and top left for the three sets of images, respectively.

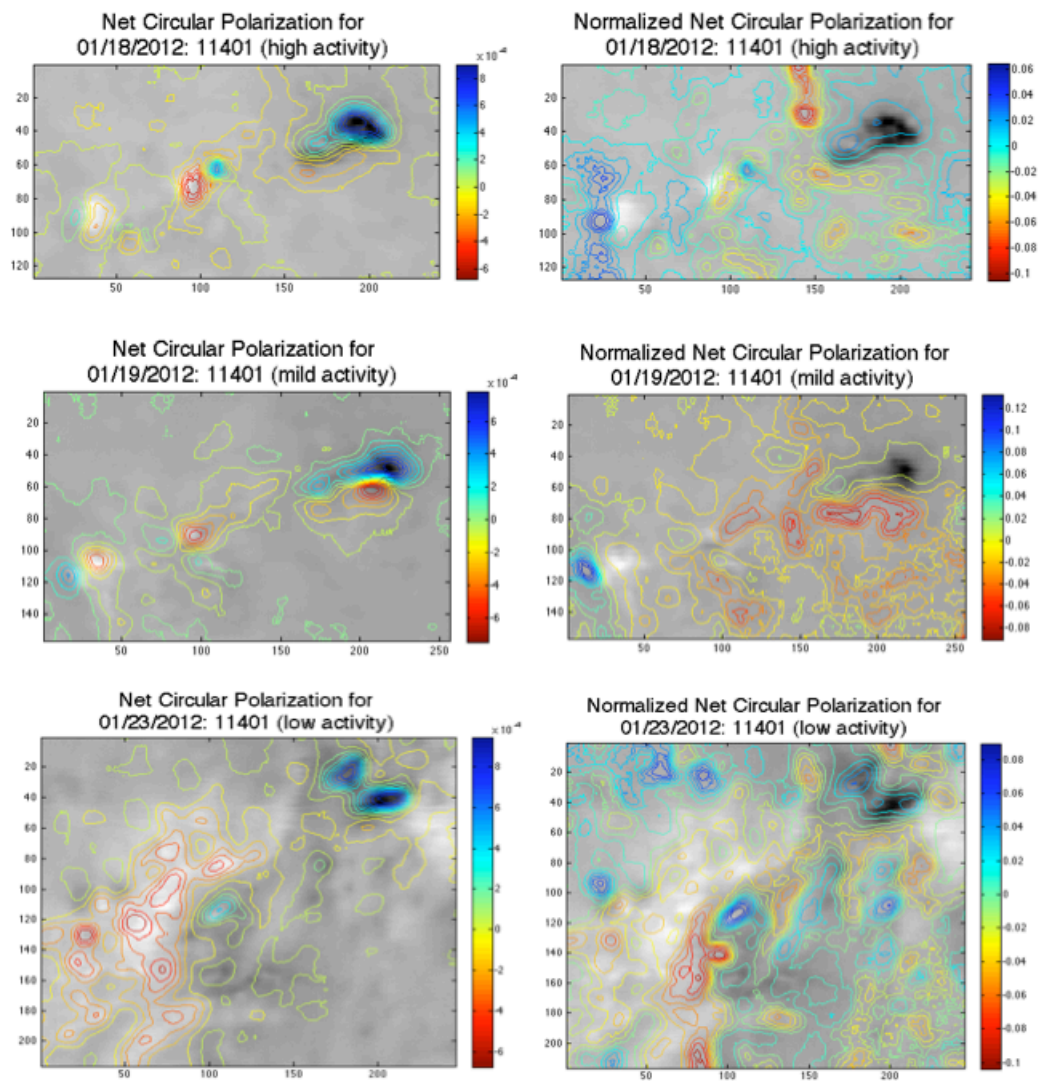


Figure 4.10: Images constructed of NOAA 11401 from Stokes V with contour maps of net circular polarization corresponding to spatial points for three separate days and activity. Disk-center is to the top right, top right, and top left for the three sets of images, respectively.

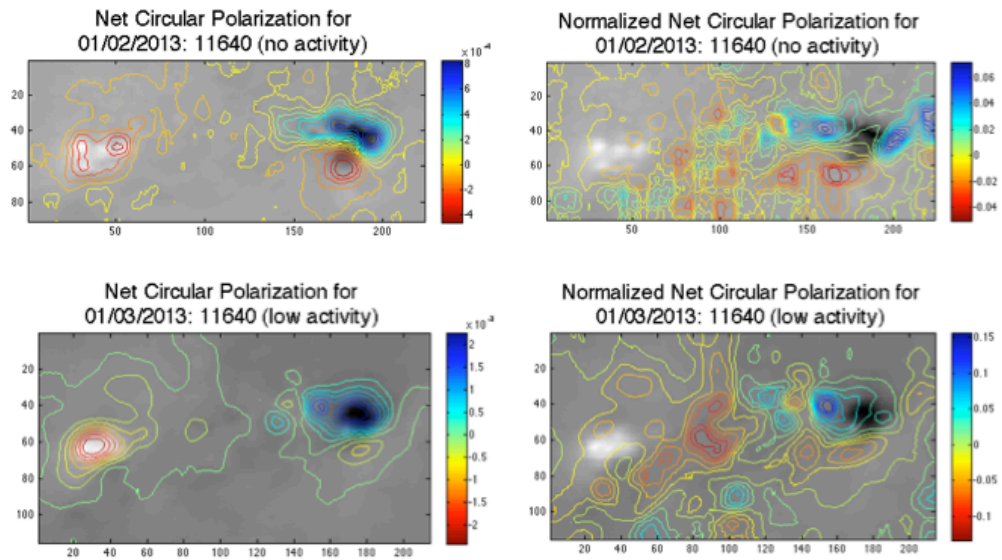


Figure 4.11: Images constructed of NOAA 11640 from Stokes V with contour maps of net circular polarization corresponding to spatial points for two separate days and activity. Disk-center is to the top left for both sets of images.

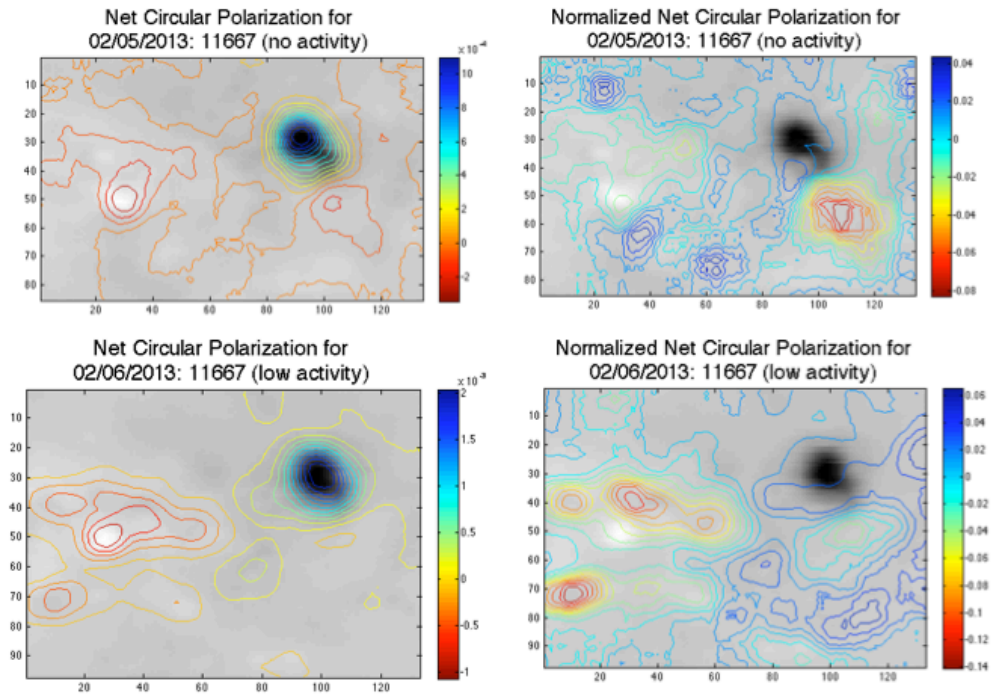


Figure 4.12: Images constructed of NOAA 11667 from Stokes V with contour maps of net circular polarization corresponding to spatial points for two separate days and activity. Disk-center is to the top right, and directly upwards for the two sets of images, respectively.

Again, the contour maps corresponding to high solar flare activity yield the most distinct contrast between positive and negative values. Therefore, comparison between B_{LOS} and both ncp and NCP is presented in Figures 4.13 through 4.16. Much like area asymmetry, the normalized net circular polarization exhibits a predictable trend: symmetric V profiles yielding low NCP at high magnetic field strength and anomalous, asymmetric V profiles yielding high NCP at low magnetic field strength. There is a slight negative tendency, with NCP for $|B_{LOS}| > 200$ G having the opposite sign as the corresponding B_{LOS} . This inclination becomes more apparent in lower solar flare activity data.

Unlike any of the previous observations in this contribution or those preceding it, an intriguing relationship between ncp and B_{LOS} is seen. The following Figures show a clear odd-powered proportionality, with $ncp \sim (-B_{LOS})^p$ for some odd p-value. According to Almeida & Lites (1992), net circular polarization depends on the product of gradients in velocity and field inclination, resulting in second-order terms. Though the results below indicate higher than second-order, nonlinear dependence is directly observed. Not only is ncp affected by the inclination of the magnetic field, it is also affected by the velocity of the magnetized plasma. This dual dependence relates to the magnetic flux, or the magnetic filling factor.

Another factor that can increase profile asymmetry, ncp, and the value of p can be temperature within different regions and emission sources (Martinez-Sykora et al. 2011). More specifically, the temperature within the flux tubes, which is dependent on the amount of magnetic flux (Zayer et al. 1990). For example, assuming the strongest magnetic field values relate to the positive and negative sunspot poles, their angle of

inclination will be $\pm 90^\circ$ (directly out of and into the solar surface). Therefore, not only do we observe the higher magnetic field with a higher filling factor and temperature, but also a more direct line-of-sight.

The nonlinear dependence of ncp on B_{LOS} increases with solar flare activity, reinforcing the role played by magnetic flux. The Figures show as flare activity either decreases or increases, nonlinearity responds accordingly. This can be thought of as a response to either organized or disorganized field gradients along the line-of-sight. Higher activity leads to a more unified flow field out of the sunspot and back into the penumbra. Thus, more symmetric Stokes V profiles will occur with less net circular polarization and vice-versa. Furthermore, the $|B_{\text{LOS}}| < 200$ G region associated with neither the umbra nor penumbra does not give predominantly meaningless high-value results as in the NCP, area asymmetry, and amplitude asymmetry plots. Here, the central ncp region is in agreement with the high B_{LOS} , outer ncp. This central region also becomes more rotated with a more negative slope as solar flare activity decreases, strengthening the relationship between nonlinearity and solar flare activity.

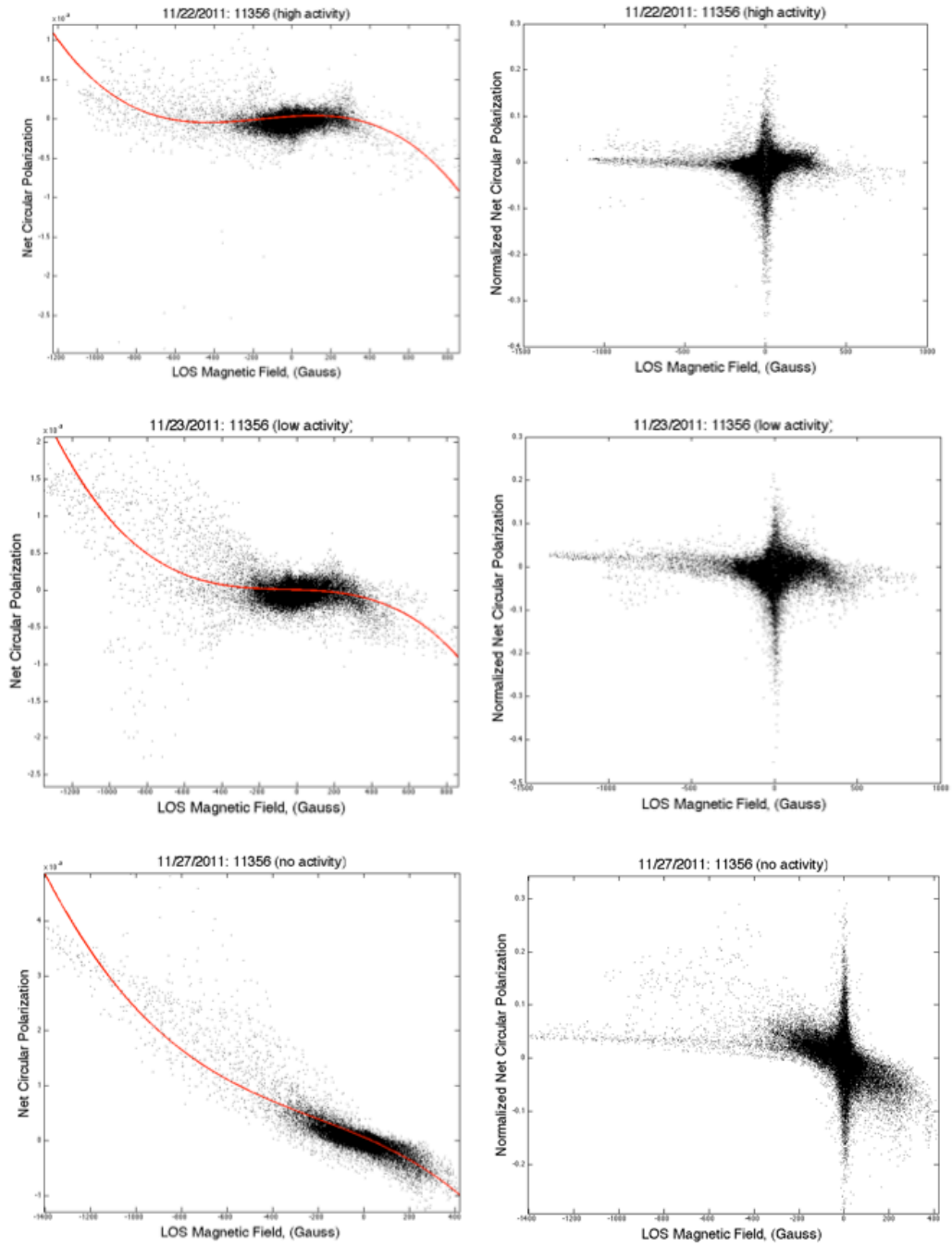


Figure 4.13: Net circular polarization versus line-of-sight magnetic field for NOAA 11356 in three separate days and activity with trend lines.

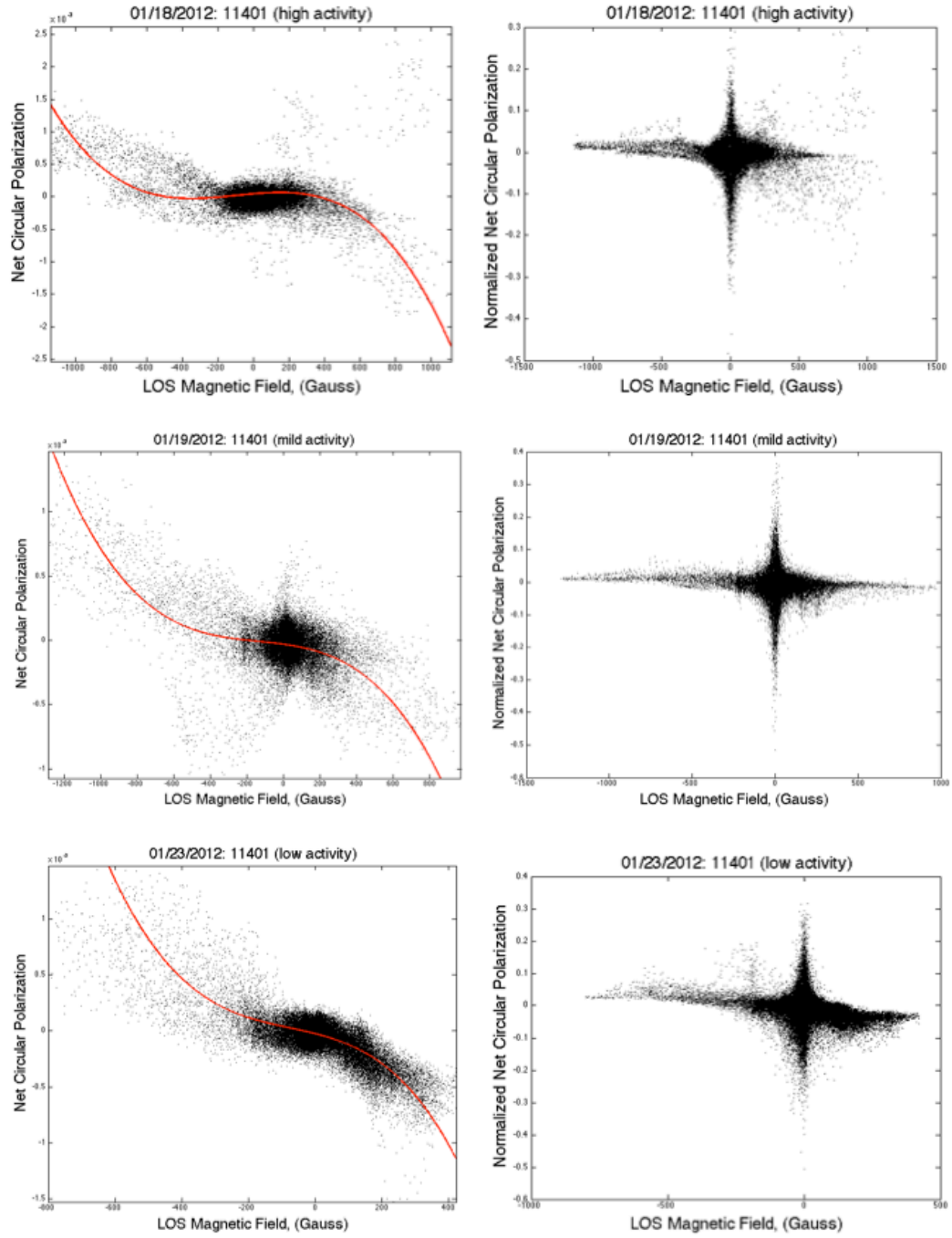


Figure 4.14: Net circular polarization versus line-of-sight magnetic field for NOAA 11401 in three separate days and activity with trend lines.

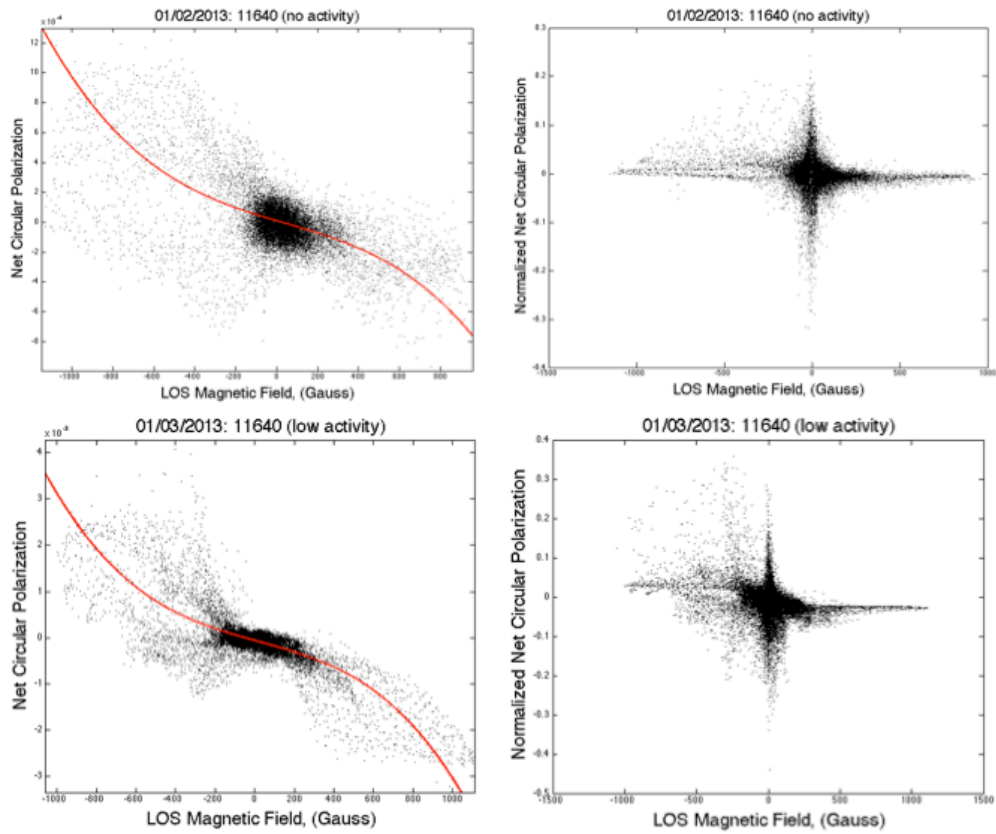


Figure 4.15: Net circular polarization versus line-of-sight magnetic field for NOAA 11640 in two separate days and activity with trend lines.

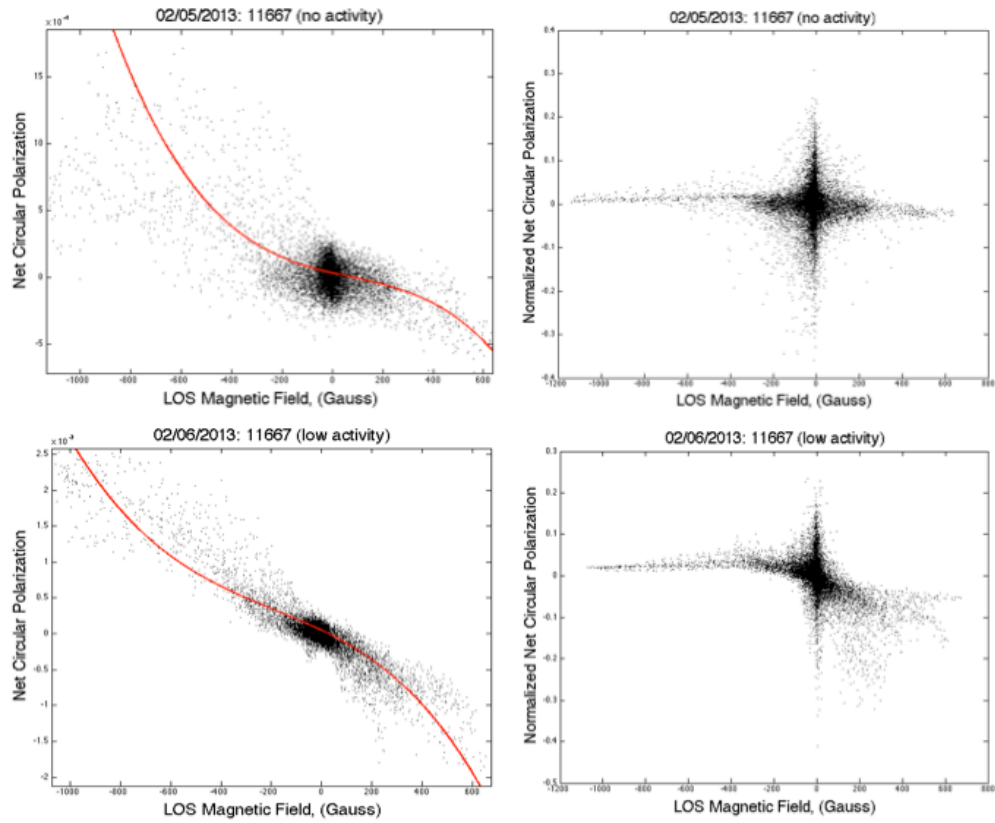


Figure 4.16: Net circular polarization versus line-of-sight magnetic field for NOAA 11667 in two separate days and activity with trend lines.

4.3 Weak-Field Approximation

Surprisingly, much less has been done to quantitatively correlate observed Stokes profiles with the observed B_{LOS} . Using equation 3.7, the Zeeman effect in a weak field may be modeled (Harvey, 1985). This contribution seeks to produce the constant k in equation 3.9 for all days, field strengths, and activity within the data set. In the following results, it can be seen that even with high field strength, Γ_R is linearly associated with B_{LOS} and agrees with J. Harvey's equation. Γ_P is not linearly dependent on B_{LOS} . It appears to be parabolic, or at least proportional to some power of B_{LOS} which is greater than 1.

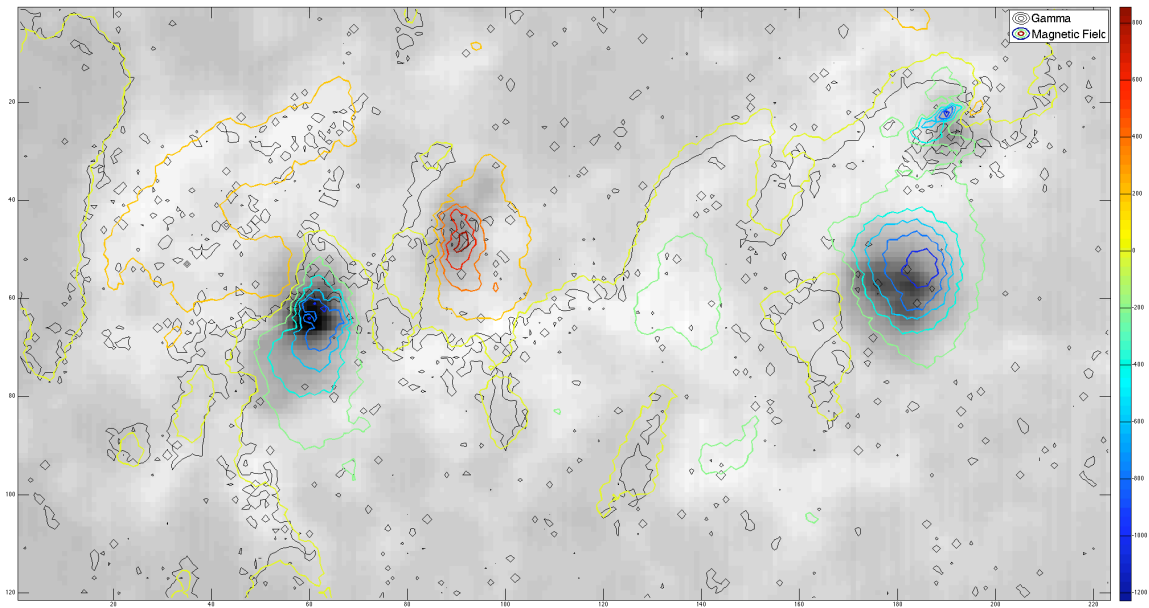


Figure 4.17: Sample image of Stokes V with superimposed contour maps of line-of-sight magnetic field (colored) and derived gamma (black).

Figure 4.17 illustrates how connected Γ and B_{LOS} are, especially near the neutral lines shown in yellow. To reiterate, B_{LOS} shown in color is a provided quantity from the VSM. Γ , shown in black, is derived from the Stokes V and I, also provided by the VSM. It is a logical step to observe this connection quantitatively. From the linearity of

equation 3.9, plotting corresponding spatial values of Γ vs. B_{LOS} should render k . From Figures 4.18 through 4.21, an average value for k has been determined to be $(23.7 \pm 4.76) \times 10^{-5}$ (Angstrom/Tesla).

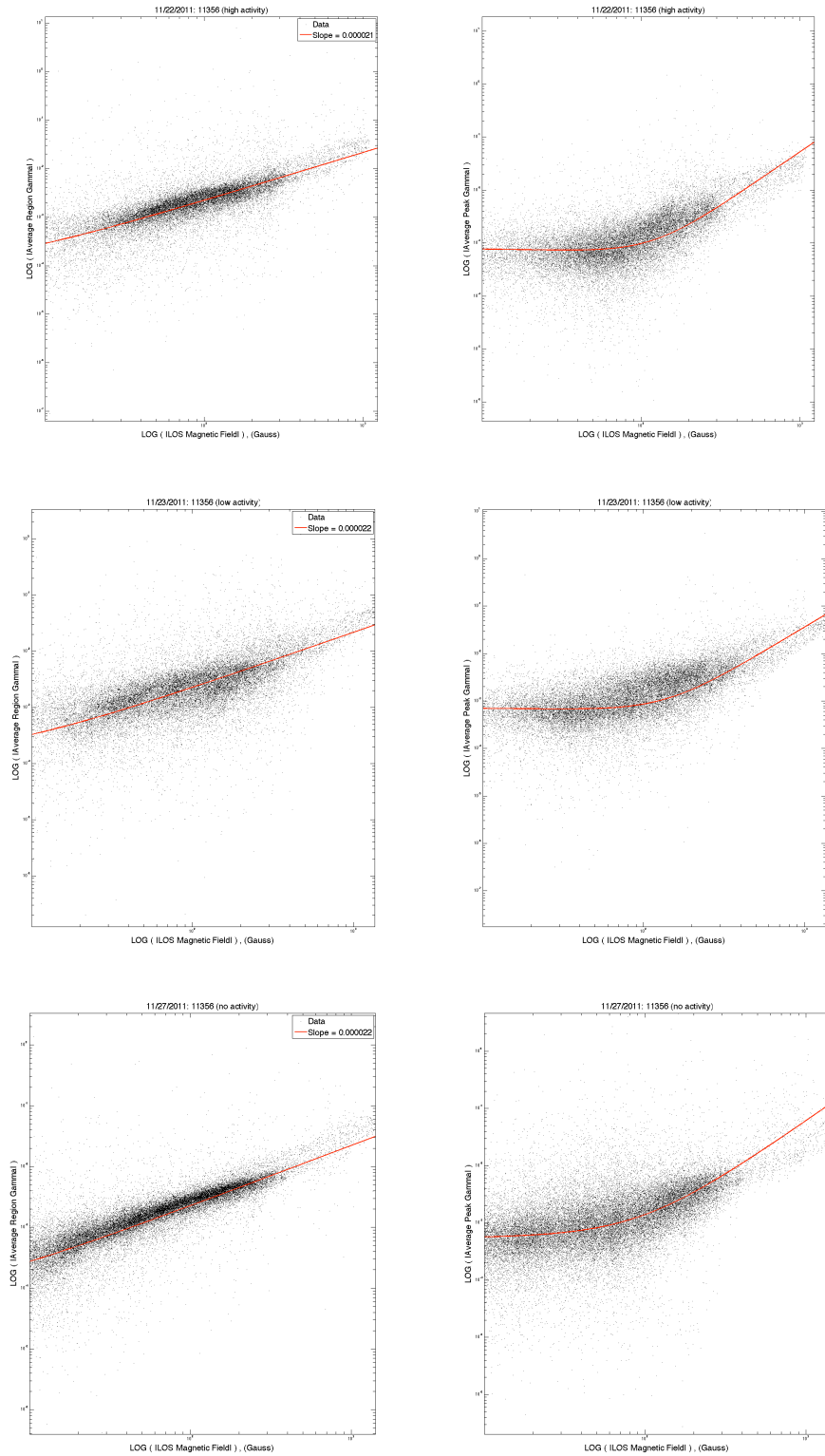


Figure 4.18: Gamma versus line-of-sight magnetic field for NOAA 11356 in three separate days and activity with trend lines.

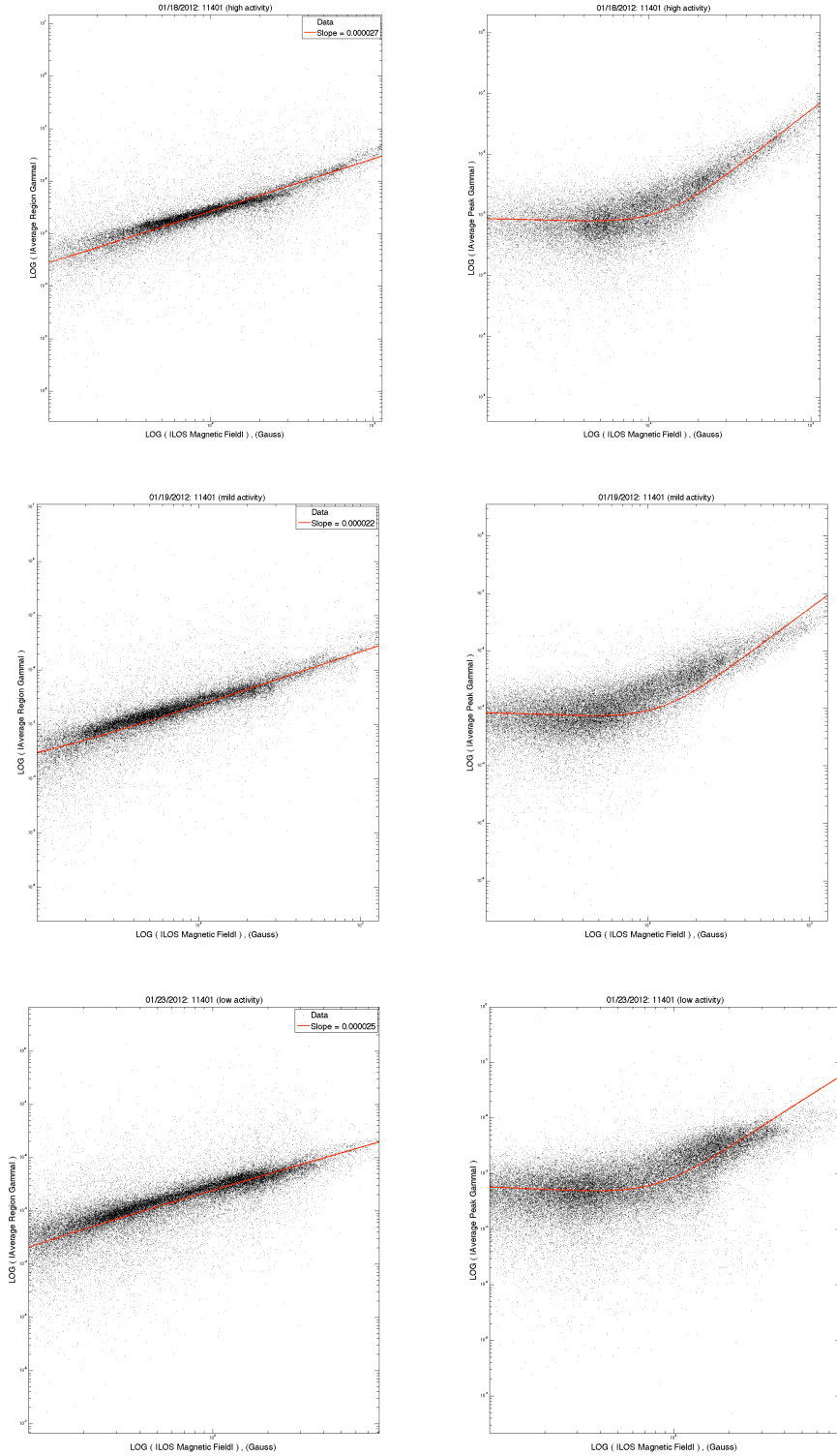


Figure 4.19: Gamma versus line-of-sight magnetic field for NOAA 11401 in three separate days and activity with trend lines.

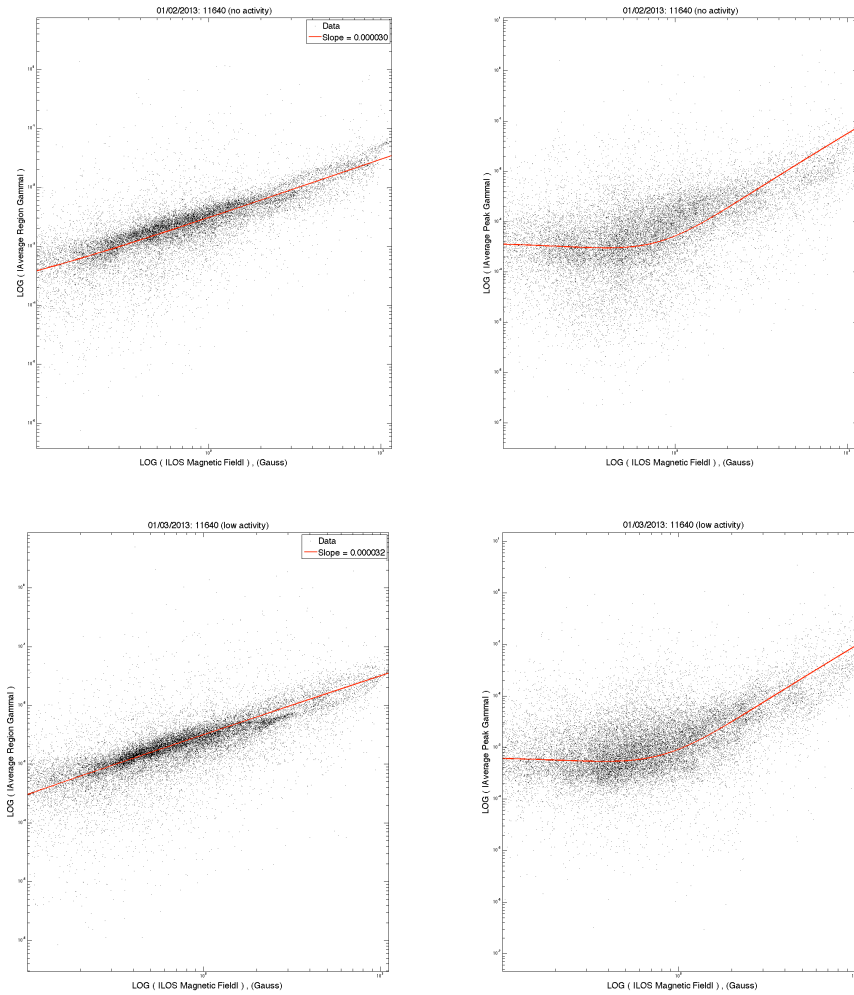


Figure 4.20: Gamma versus line-of-sight magnetic field for NOAA 11640 in two separate days and activity with trend lines.

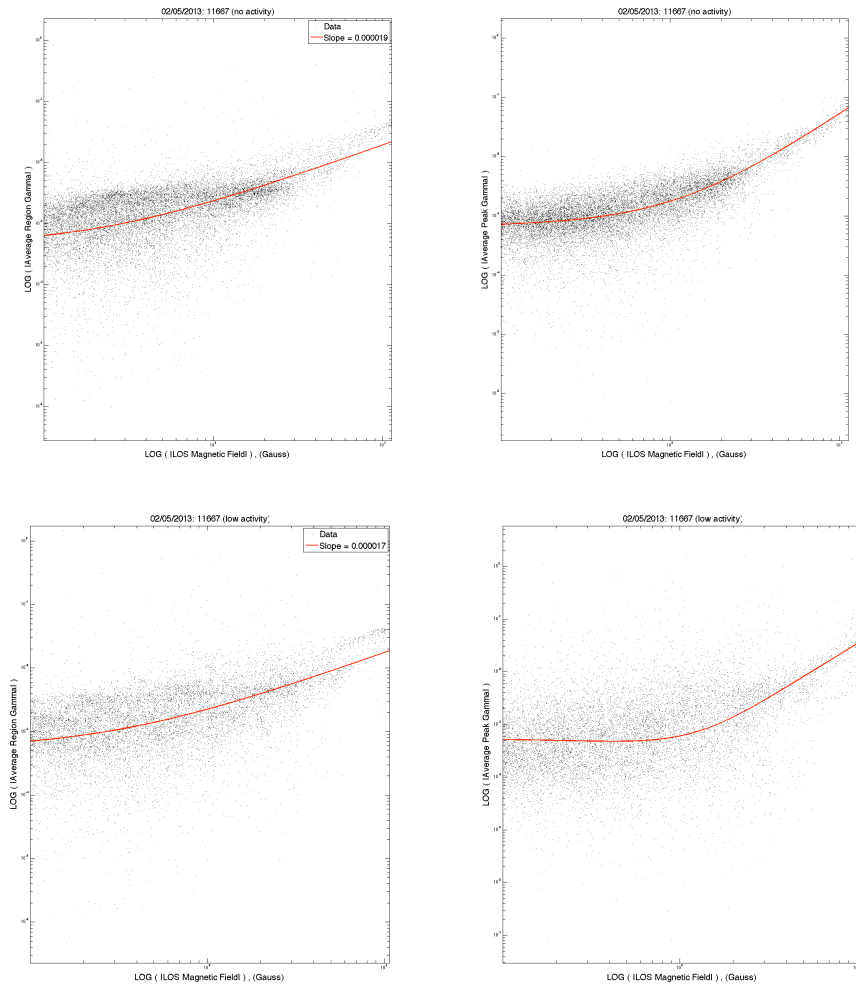


Figure 4.21: Gamma versus line-of-sight magnetic field for NOAA 11667 in two separate days and activity with trend lines.

Chapter 5

Conclusion

In this study of Stokes V and I profiles, properties of interest have been compared to the line-of-sight magnetic field. Described are methods of evaluation used in previous works for area and amplitude asymmetry as well as net circular polarization. Also, a method introduced by Harvey (1985) to relate V and $dI/d\lambda$ by a linear constant. The results have agreed with expectations put forward by numerous works that have investigated similar aspects of Zeeman-induced polarization of atomic spectra. Results have also revealed new characteristics of the observed properties.

Observed asymmetry values agree strongly with cited research. Center and limb-side penumbrae adhere to the theoretical results based on line-of-sight and the Evershed flow (Gosain & Choudhary, 2003). Contradicting the vast congruency of property characteristics is the multiple correlations observed between asymmetry and solar flare activity. It is conceivable, and likely, that the mechanisms powering solar flares are not solely responsible for producing asymmetries. The more surprising aspect is observed when less solar flare activity coincides with more asymmetry. Granted, this is only seen to occur in regions with overall low activity, but still begs further investigation.

Net circular polarization is arguably the most revealing component of Stokes V. Some deviations from previous findings, such as observed symmetry about the connection between disk-center and sunspot-center (Tritschler et al. 2007), were detected but overall agreements similar to those in the asymmetry results maintain the reliability of the derived data. Previously unseen nonlinearity is detected between net circular polarization and the line-of-sight magnetic field, which responds to varying solar flare

activity. Multiple causes have been suggested (Zayer et al. 1990; Martinez-Sykora et al. 2011), but further study is ultimately needed to reveal the exact nature of this dependence and to pinpoint its cause.

Finding linear relationships in nature is always an ambitious task. Harvey's weak-field approximation method of relating Stokes V and I with magnetic-field strength does exactly that. The data analyzed to produce the results in Section 4.3 confidently confirms this method for the first time. There is a relatively large spread in the obtained average linear constant, $k = (23.7 \pm 4.76) \times 10^{-5}$ (Angstrom/Tesla). This is due to the varying slope of Γ vs. B_{LOS} throughout different levels of solar flare activity. A total average value as listed may therefore require further considerations.

With space-based observations of high activity sunspots at solar-disk center, it is proposed that further research would be able to conduct similar experimentation and answer the questions left behind: a better grasp of the relationship between asymmetry and solar flare activity, net circular polarization and line-of-sight magnetic fields, and a more reliable value for Harvey's linear constant.

References

1. Almeida, J. S., Lites B. W. 1992, ApJ, 398, 359.
2. Aznar Cuadro, R. & Jeffrey, C. S. 2002, A&A, 385, 131.
3. Balasubramaniam, K. S., Kiel, S. L., & Tomczyk, S. 1997, ApJ, 482, 1065.
4. Balasubramaniam, K. S. & Pevstov, A. A., 2011, Proc. SPIE 8148, 814809.
5. Beck, C. 2013, A&A, arXiv preprint arXiv:1010.2095.
6. Borrero, J. M., Bellot Rubio, L. R., Müller, D. A. N. 2007, ApJ, 666, L133.
7. Borrero, J. M., Solanki, S. K. 2010, ApJ, 709, 349.
8. Choudhary, D. P., Balasubramaniam, K. S. 2007, ApJ, 664, 1228.
9. Choudhary, D. P., Balasubramaniam, K. S., Yoshinori Suematsu. 2004, ASP Conference Series, Vol. 325.
10. Choudhary, D. P., Venkatakrishnan, P., Gosain, S. 2002, ApJ, 573, 851.
11. De la Cruz Rodriguez, J. 2010, Ph.D. thesis, Stockholm, Univ.
12. De Pontieu, B., McIntosh, S. W., Carlsson, M., Hansteen, V. H., Tarbell, T. D., Boerner, P., Martínez-Sykora, J., Schrijver, C. J., Title, A. M. 2011, Science, 331.6013, 55.
13. Deng, N., Choudhary, D. P., Balasubramaniam, K. S. 2010, ApJ, 719, 385.
14. Deng, N., Choudhary, D. P., Tritschler, A., Denker, C., Liu, C., Wang, H. 2007, ApJ, 671, 1013.
15. Deng, Na. "ASP Observations on 2001 October 16 & 17 at NSO/SP". *Na Deng's Work Page*. 2007. March 24, 2014. <http://solar.njit.edu/~nd7/asp2001/>.
16. Dennis, Brian & Milligan, Ryan. "Solar Satellites". Revision #130007. *Scholarpedia*. March 24, 2014. http://www.scholarpedia.org/article/Solar_Satellites.
17. Fennell, Jeff. "The Sun's Chromosphere: Definition, Temperature & Facts." *Education Portal*. March 24, 2014. <http://education-portal.com/academy/lesson/the-suns-chromosphere-definition-temperature-facts.html#lesson>.
18. Garfinkle, David & Garfinkle, Richard. *Three Steps to the Universe: From the Sun to Black Holes to the Mystery of Dark Matter*. University of Chicago Press, 2008. Print.
19. Gosain, S., Choudhary, D. P. 2003, Solar Physics, 271, 119.

20. Gouttebroze, P. & Heinzel, P. 2002, *A&A*, 385, 273.
21. Grossman-Doerth, U., Schüssler, M., Sigwarth, M., & Steiner, O. 2000, *A&A*, 357, 351.
22. Hudson, H. S., Fisher, G. H., & Welsch, B. T. 2008, in *ASP Conf. Ser. 383 Subsurface and Atmospheric Influences on Solar Activity*, ed. R. Howe et al. (San Francisco, CA: ASP), 221.
23. Harvey, J. W. 1985, *Measurements of Solar Vector Magnetic Fields*, 1, 109.
24. Jess, D. B., Pascoe, D. J., Christian, D. J., Mathioudakis, M., Keys, P. H., Keenan, F. P. 2012, *ApJL*, 744.1: L5.
25. Jess, D. B., Mathioudakis, M., Erdélyi, R., Crockett, P. J., Keenan, F. P., Christian, D. J. 2009, *Science*, 323.5921, 1582.
26. Kneale, Ruth. "Vector Spectromagnetograph". *NSO/Synoptic Program*. 06 July 2013. 12 March 2014. <http://solis.nso.edu/VSMOverview.html>.
27. Lomb, N. "Sunspots and Magnetic Fields – When did Scientists Discover the Connection". *Sydney Observatory*. April 14, 2014. <http://www.sydneyobservatory.com.au/2011/sunspots-and-magnetic-fields---when-did-scientists-discover-the-connection/>
28. Martínez-Sykora, J., De Pontieu, B., Hansteen, V., McIntosh, S. W. 2011, *ApJ*, 732, 84.
29. McIntosh, S. W., De Pontieu, B., Carlsson, M., Hansteen, V., Boerner, P., Goossens, M. 2011, *Nature*, 475, 477.
30. Nave, C. R. "Zeeman Effect in Hydrogen". *Hyperphysics*. April 14, 2014. <http://hyperphysics.phy-astr.gsu.edu/hbase/quantum/zeeman.html>.
31. Parker, E. N. 1988, *ApJ*, 330, 474.
32. Pietarila, A., Socas-Navarro, H., Bogdan, T. 2007, *ApJ*, 670, 885.
33. Priest, E. R., Schrijver, C. J. 1999, *Solar Physics*, 190.1-2, 1.
34. Rumberg, Jennifer. "Solar Storm and Space Weather – Frequently Asked Questions". March 24, 2014. *NASA*. http://www.nasa.gov/mission_pages/sunearth/spaceweather/index.html#q3
35. Sigwarth, M. 2001, *ApJ*, 563, 1031.
36. Smith, G. & Drake, J. J. 1988, *Royal Astronomical Society*, 231, 115.
37. Socas-Navarro, H., Trujillo Bueno, J., Ruiz Cobo, B. 2000, *ApJ*, 544, 1141.
38. Solanki, S. K. 1986, *A&A*, 168, 311.

39. Solanki, S. K., Pahlke, K. D. 1988, A&A, 201, 143.
40. Solanki, S. K., Stenflo, J. O. 1984, A&A, 148, 123.
41. "Stokes Parameters". *Wikipedia*. March 24, 2014.
http://en.wikipedia.org/wiki/Stokes_parameters.
42. Sturrock, P. A. 1999, ApJ, 521, 451.
43. "The Magnetic Field of the Sun". March 24, 2014.
<http://csep10.phys.utk.edu/astr162/lect/Sun/magnetic.html>.
44. Tritschler, A., Müller, D. A. N., Schlichenmaier, R., Hagenaar, H. J. 2007, ApJ, 671, L85.
45. Zayer, I., Stenflo, J. O., Keller, C. U., & Solanki, S. K. 1990, A&A, 239, 356.

Appendix

```
1. %Read in the entire folder.
2. fileList = getAllFiles('/Users/maxnorris/Desktop/20130205'); **
3. %Provide title for future plots.
4. regions={' 02/05/2013: 11667 (no activity) '};
5. %Remove unwanted directory file.
6. if strcmp(fileList{1}(35:end),'.DS_Store')==1
7.     fileList=fileList(2:end);
8. end
9. %Preallocate Stokes matrices.
10. I=zeros(128,2048,2047);
11. V=zeros(128,2048,2047);
12. I_image=zeros(2047,2048);
13. V_image=zeros(2047,2048);
14. %Create the matrices from VSM data.
15. for n=1:2047
16.     %File name.
17.     f=fileList{n};
18.     %Turn the file name into a readable string.
19.     f=sprintf(f);
20.     %Read in the entire fits file.
21.     a=fitsread(f);
22.     %Make I and V matrices.
23.     I(:, :, n)=a(:, :, 1);
24.     V(:, :, n)=a(:, :, 2);
25.     %Make a solar image using average values across all wavelengths.
26.     I_image(n, :)=mean(I(:, :, n));
27.     V_image(n, :)=mean(V(:, :, n));
28.     %Clear variables for next file.
29.     clear a f r m
30.     %Print file number to indicate progress.
31.     fprintf('%0f\n',n)
32. end
33. %Images to be used.
34. IplusV=I_image+V_image;
35. IminusV=I_image-V_image;
36. %Show the image to select locations.
37. imagesc(IplusV)
38. colormap(gray)
39. %Select location(s).
40. fprintf('\nSelect sunspot region, starting with \nlower left corner and
ending in the upper right.\n')
41. [x,y]=ginput(2);
42. x=round(x);
43. y=round(y);
44. %Create vectors for interpolation.
```

```

45.     xx=1:01:128;
46.     lambda=(8542-2.275):(4.55/12700):(8542+2.275);
47.     n=1;
48.     %Create cells for the V columns and close-ups.
49.     vSpot=V(:,x(2*n-1):x(2*n),y(2*n):y(2*n-1));
50.     vCol{n}=vSpot;
51.     iSpot=I(:,x(2*n-1):x(2*n),y(2*n):y(2*n-1));
52.     iCol{n}=iSpot;
53.     spotImage=IplusV(y(2*n):y(2*n-1),x(2*n-1):x(2*n));
54.     imCol{n}=spotImage;
55.     %Set wavelength zone to be looked at.
56.     ind60=5901; %xx=60
57.     ind80=7901; %xx=80
58.     %Interpolate V and I at each spatial point to evaluate certain quantities.
59.     for z=1:x(2)-x(1)+1
60.     for b=1:y(1)-y(2)+1
61.     for p=1:128
62.         v3(p)=vCol{n}(p,z,b); %V profile at each pixel.
63.         i3(p)=iCol{n}(p,z,b); %I profile at each pixel.
64.     end
65.     Vinterp=interp1(1:128,v3,xx); %interpolated V at each pixel.
66.     Iinterp=interp1(1:128,i3,xx); %interpolated I at each pixel.
67.     d_i=diff(Iinterp); %Change in I with wavelength.
68.     gamma2(b,z,:)=Vinterp(1:end-1)./d_i; %Gamma = V/I
69.     ncp(b,z)=sum(Vinterp)*(lambda(2)-lambda(1)); %net circular polarization
70.     %normalized net circular polarization
71.     ncpNorm(b,z)=sum(Vinterp./max(max(Vinterp)))*(lambda(2)-lambda(1));
72.     mf=minindex(Vinterp(ind60:ind80)); %minimum between mid range **
73.     mF=maxindex(Vinterp(ind60:ind80)); %maximum between mid range **
74.     m1=min(mf,mF)+ind60-1; %first extreme
75.     m2=max(mf,mF)+ind60-1; %second extreme
76.     zero_point(b,z,n)=minindex(abs(Vinterp(m1:m2)))+m1-1; %zero-
77.     crossing
78.     B=sum(abs(Vinterp(1:zero_point(b,z,n)))); %blue area
79.     R=sum(abs(Vinterp(zero_point(b,z,n):end))); %red area
80.     A_area(b,z,n)=100*(B-R)/(B+R); %Area Asymmetry
81.     ab=abs(Vinterp(m1)); %blue amp
82.     ar=abs(Vinterp(m2)); %red amp
83.     A_amp(b,z,n)=100*(ab-ar)/(ab+ar); %Amplitude Asymmetry
84.     end
85.     end
86.     asym_area{n}=A_area;
87.     aSmooth_area{n}=smooth2a(asym_area{n},5,5); %smoothed area
88.     asymmetry for contour map **
89.     asym_amp{n}=A_amp;
90.     aSmooth_amp{n}=smooth2a(asym_amp{n},5,5); %smoothed amplitude

```

```

asymmetry for contour map
87. spot=1;
88. %View sunspot region to select sunspot and surrounding region pixels.
89. imagesc(imCol{spot})
90. colormap(gray)
91. counter=1;
92. %Zero's to plot.
93. for n=1:length(xx)
94. zz(n)=0;
95. end
96. %Sunspot selection and its Stokes profiles.
97. while counter==1
98. figure(1)
99. fprintf('Select Sunspot Location\n');
100. [x1,y1]=ginput(1);
101. x2=round(x(2*spot-1)+x1);
102. y2=round(y(2*spot)+y1);
103. for p=1:128
104. vv(p)=V(p,x2,y2);
105. ii(p)=I(p,x2,y2);
106. end
107. VinterpSpot=interp1(1:128,vv,xx); %interpolated V at sunspot pixel
108. IinterpSpot=interp1(1:128,ii,xx); %interpolated I at sunspot pixel
109. mfSpot=minindex(VinterpSpot(ind60:ind80)); %V minimum between mid
range
110. mFSpot=maxindex(VinterpSpot(ind60:ind80)); %V maximum between
mid range
111. m1Spot=min(mfSpot,mFSpot)+ind60-1; %V first extreme
112. m2Spot=max(mfSpot,mFSpot)+ind60-1; %V second extreme
113. %Sunspot zero-crossing.
114. zero_pointSpot=minindex(abs(VinterpSpot(m1Spot:m2Spot)))+m1Spot-1;
115. %Verify location.
116. figure(2)
117. hold off
118. plot(xx,VinterpSpot)
119. axis('tight')
120. hold on
121. plot((zero_pointSpot*.01)+1,VinterpSpot(zero_pointSpot),'ko')
122. plot(xx,zz,'m--')
123. conf=input('Is this ok? (y/n)\n','s');
124. if conf=='y'
125. vSpotConf=VinterpSpot;
126. zeroCrossSpot=zero_pointSpot;
127. counter=2;
128. close all
129. else

```

```

130.     counter=1;
131.     clear vv VinterpSpot mfSpot mFSpot m1Spot m2Spot zero_pointSpot
132.     end
133.     end
134.     imagesc(imCol{spot})
135.     colormap(gray)
136.     counter=1;
137.     %Surrounding region selection and its Stokes profiles.
138.     while counter==1
139.         figure(1)
140.         imagesc(imCol{spot})
141.         colormap(gray)
142.         counter=1;
143.         fprintf('Select Active Region Location\n');
144.         [x3,y3]=ginput(1);
145.         x4=round(x(2*spot-1)+x3);
146.         y4=round(y(2*spot)+y3);
147.         for p=1:128
148.             vv(p)=V(p,x4,y4);
149.             ii(p)=I(p,x4,y4);
150.         end
151.         VinterpRegion=interp1(1:128,vv,xx); %interpolated V at region pixel.
152.         IinterpRegion=interp1(1:128,ii,xx); %interpolated I at region pixel.
153.         mfRegion=minindex(VinterpRegion(ind60:ind80)); %minimum between
154.         mFRegion=maxindex(VinterpRegion(ind60:ind80)); %maximum between
155.         m1Region=min(mfRegion,mFRegion)+ind60-1; %first extreme
156.         m2Region=max(mfRegion,mFRegion)+ind60-1; %second extreme
157.         %Region zero-crossing.
158.         zero_pointRegion=minindex(abs(VinterpRegion(m1Region:m2Region)))+
159.         m1Region-1;
160.         %Verify location.
161.         figure(2)
162.         hold off
163.         plot(xx,abs(VinterpRegion))
164.         hold on
165.         plot((zero_pointRegion*.01)+1,VinterpRegion(zero_pointRegion),'ko')
166.         axis('tight')
167.         conf=input('Is this ok? (y/n)\n','s');
168.         if conf=='y'
169.             vRegionConf=VinterpRegion;
170.             zeroCrossRegion=zero_pointRegion;
171.             f2 **
172.             hold off
173.             plot(abs(VinterpRegion))

```

```

173.      %Identify core and wing regions.
174.      fprintf('Select end of blue region and start of red.\n')
175.      [xbend,ybend]=ginput(2);
176.      xbend=round(xbend);
177.      counter=2;
178.      close all
179.      else
180.      counter=1;
181.      clear vv VinterpRegion mfRegion mFRegion m1Region m2Region
zero_pointRegion
182.      end
183.      end
184.      close all
185.      %Select quiet-Sun location.
186.      counter=1;
187.      while counter==1
188.      figure(1)
189.      imagesc(IplusV)
190.      colormap(gray)
191.      fprintf('Select Quiet Region Location\n');
192.      [x5,y5]=ginput(1);
193.      x6=round(x5);
194.      y6=round(y5);
195.      for p=1:128
196.      vv(p)=V(p,x6,y6);
197.      ii(p)=I(p,x6,y6);
198.      end
199.      VinterpQuiet=interp1(1:128,vv,xx); %interpolated V at quiet pixel.
200.      IinterpQuiet=interp1(1:128,ii,xx); %interpolated I at quiet pixel.
201.      mfQuiet=minindex(VinterpQuiet(ind60:ind80)); %minimum between mid
range
202.      mFQuiet=maxindex(VinterpQuiet(ind60:ind80)); %maximum between
mid range
203.      m1Quiet=min(mfRegion,mFQuiet)+ind60-1; %first extreme
204.      m2Quiet=max(mfRegion,mFQuiet)+ind60-1; %second extreme
205.      %Quiet-Sun zero-crossing.
206.      zero_pointQuiet=minindex(abs(VinterpQuiet(m1Quiet:m2Quiet)))+m1Qu
iet-1;
207.      counter=2;
208.      end
209.      %Normalized v profiles
210.      vNorm_spot=vSpotConf./max(abs(vSpotConf));
211.      vNorm_region=vRegionConf./max(abs(vRegionConf));
212.      %Normalized absolute v profiles for gaussian fits
213.      vAbsNorm_spot=abs(vSpotConf)./max(abs(vSpotConf));
214.      vAbsNorm_region=abs(vRegionConf)./max(abs(vRegionConf));

```

```

215. %lorentzian fits
216. Ls=lorentzfit(lambda,vAbsNorm_spot); **
217. Lr=lorentzfit(lambda,vAbsNorm_region);
218. %Determine the polarization state of V.
219. if pyr>pyb
220. flip2=-1;
221. else
222. flip2=1;
223. end
224. close all
225. clear P S MU lamHat regionP regionC Lc Pslope bb Lp gc gp voigtC
voigtP Vapprox Lapprox Gapprox
226. %Create blue and red regions of Stokes V.
227. regionP=zz;
228. regionP(1:pxb)=vAbsNorm_region(1:pxb);
229. regionP(pxr:end)=vAbsNorm_region(pxr:end);
230. pZone=[vAbsNorm_region(1:pxb) vAbsNorm_region(pxr:end)];
231. pNorm=max(pZone);
232. regionC=zz;
233. regionC(pxb+1:pxr-1)=vAbsNorm_region(pxb+1:pxr-1);
234. Pslope=(regionP(pxb)-regionP(pxr))/(lambda(pxb)-lambda(pxr));
235. bb=regionP(pxb)-Pslope*lambda(pxb);
236. regionP(pxb+1:pxr-1)=bb+Pslope.*lambda(pxb+1:pxr-1);
237. %Lorentz fit
238. [Lp LpParams]=lorentzfit(lambda,regionP);
239. [Lc LcParams]=lorentzfit(lambda,regionC);
240. clear Lc
241. lamSig=lambda-lambda(zero_pointRegion);
242. Lc=LcParams(1)/(((lamSig.*2).^2)+LcParams(3))+LcParams(4);
243. Lc=Lc+abs(min(Lc));
244. vPnorm=pNorm/max(abs(vPsmooth3));
245. %Find zero-crossing wavelengths for sunspot, photospheric region
contribution, and chromospheric region contribution based on the
Lorentzian profiles.
246. spotZero=lambda(zeroCrossSpot);
247. photoZero=lambda(maxindex(Lp));
248. chromoZero=lambda(maxindex(Lc));
249. zeroCross=[spotZero,photoZero,chromoZero];
250. %Eliminate gap in VSM image as well as bordering zones.
251. imagesc(IplusV)
252. colormap(gray)
253. fprintf('Select edges of solar disk in this order: right, top, left, bottom.\n')
254. [xlim,ylim]=ginput(4);
255. xlim=round(xlim);
256. ylim=round(ylim);
257. newDisk=IplusV;

```

```

258.     newDisk(:,948:1033)=[];
259.     newDisk(:,xlim(1):end)=[];
260.     newDisk(:,1:xlim(3))=[];
261.     newDisk=rot90(newDisk);
262.     newDisk(:,ylim(4):end)=[];
263.     newDisk(:,1:ylim(2))=[];
264.     newDisk=rot90(newDisk,3);
265.     close all
266.     %Find the wavelength limits for gamma.
267.     minlim=min([zero_pointSpot-1000 zero_pointRegion-1000
zero_pointQuiet-1000]);
268.     maxlim=max([zero_pointSpot+1000 zero_pointRegion+1000
zero_pointQuiet+1000]);
269.     %Find the best wavelength to image Stokes V in contour maps based on
level of contrast.
270.     for n=1:128
271.         fprintf('%0f\n',n)
272.         AA=permute(V(n,:,:),[2 3 1]);
273.         AA2=AA(x(1):x(2),y(2):y(1));
274.         minA=min(AA2(:));
275.         maxA=max(AA2(:));
276.         diffA(n)=maxA-minA;
277.         clear AA AA2 AA3 minA maxA nn q
278.     end
279.     MM=maxindex(diffA);
280.     fprintf('Best Contrast at %0f\n',MM)
281.     AA=V(MM,:,:);
282.     AA2=AA(1,x(1):x(2),y(2):y(1));
283.     SS2=size(AA2);
284.     for n2=1:SS2(3)
285.         for q2=1:SS2(2)
286.             AA4(n2,q2)=AA2(1,q2,n2);
287.         end
288.     end
289.     %VSM magnetogram.
290.     vsmdisk=fitsread('/Users/maxnorris/Desktop/svsm_m1100_S2_20130205
_1546.fts');
291.     %Range gamma at each pixel.
292.     sgs=size(gamma2);
293.     for sn=1:sgs(1)
294.         for sm=1:sgs(2)
295.             gamma3(sn,sm)=mean(gamma2(sn,sm,minlim:maxlim));
296.         end
297.     end
298.     %Rotate VSM magnetogram to match Stokes I and V image.
299.     figure('color',[1,1,1])

```

```

300. subplot(1,2,1)
301. imagesc(newDisk);
302. colormap(gray)
303. title('Disk from Files','fontsize',20)
304. axis('equal')
305. axis('tight')
306. subplot(1,2,2)
307. imagesc(vsmdisk);
308. colormap(gray)
309. title('Disk from VSM','fontsize',20)
310. axis('equal')
311. axis('tight')
312. %Radii.
313. fxL=size(newDisk,2)/2;
314. fyL=size(newDisk,1)/2;
315. vxL=size(vsmdisk,2)/2;
316. vyL=size(vsmdisk,1)/2;
317. subplot(1,2,1)
318. fprintf('Select Sunspot Location from File Image\n')
319. [fx,fy]=ginput(1);
320. subplot(1,2,2)
321. fprintf('Select Sunspot Location from VSM Image\n')
322. [vx,vy]=ginput(1);
323. %Coordinates of same spatial point on both images.
324. fx2=fx-fxL;
325. fy2=fyL-fy;
326. vx2=vx-vxL;
327. vy2=vyL-vy;
328. %Radial distances.
329. fr=sqrt(fx2^2+fy2^2);
330. vr=sqrt(vx2^2+vy2^2);
331. %Angular distances to determine necessary rotation.
332. ft=mod(atan2(fy2,fx2),2*pi);
333. vt=mod(atan2(vy2,vx2),2*pi);
334. %Rotate VSM magnetogram.
335. vsmdisk2=imrotate(vsmdisk,-(vt-ft)*360/(2*pi));
336. %Eliminate remaining excess from edges.
337. vds=size(vsmdisk2,1);
338. newcut=round((vds-size(vsmdisk,1))/2)+1;
339. vsmdisk2(:,(vds-newcut+1):end)=[];
340. vsmdisk2(:,1:newcut-1)=[];
341. vsmdisk2=rot90(vsmdisk2);
342. vsmdisk2(:,(vds-newcut+1):end)=[];
343. vsmdisk2(:,1:newcut-1)=[];
344. vsmdisk2=rot90(vsmdisk2,3);
345. close all

```

```

346. %Correct the coordinates after rotation and trimming.
347. figure('color',[1,1,1])
348. subplot(2,2,1)
349. imagesc(newDisk);
350. colormap(gray)
351. title('Disk from Files','fontsize',20)
352. axis('equal')
353. axis('tight')
354. subplot(2,2,2)
355. imagesc(vsmdisk2);
356. colormap(gray)
357. title('Rotated Disk from VSM','fontsize',20)
358. axis('equal')
359. axis('tight')
360. %New x and y for rotated image.
361. [vsmnewx,vsmnewy]=ginput(1);
362. %New x for trimmed Stokes image.
363. if fx<=948-xlim(3);
364. newDiskx=x-xlim(3);
365. else
366. newDiskx=x-xlim(3)-(1033-948);
367. end
368. %Pixel-to-pixel values for line-of-sight magnetic field from VSM
magnetogram may now be compared to gamma and plotted to determine
values for k.

```

****** These functions are not found in the MatLab Library. They have either been created personally or downloaded from the MathWorks file exchange website, <http://www.mathworks.com/matlabcentral/fileexchange/>. They can be produced upon request.